



# **STRUCTURAL ANALYSIS OF A LINEAR AXIS FRAME USED IN A TURRET PUNCH PRESS**

Lappeenranta-Lahti University of Technology LUT

Master's Programme in Mechanical Engineering, Master's Thesis

2022

Atte Anttila

Examiners: Professor Timo Björk

Jussi Kosola, M.Sc. (Tech.)

## ABSTRACT

Lappeenranta-Lahti University of Technology LUT  
LUT School of Energy Systems  
Mechanical Engineering

Atte Anttila

### **Structural analysis of a linear axis frame used in a turret punch press**

Master's thesis

2022

76 pages, 44 figures and 18 tables

Examiners: Professor Timo Björk

Jussi Kosola, M.Sc. (Tech.)

Keywords: strength of materials, statics, finite element method, steel constructions

The research topic of this thesis is the structural engineering of a welded steel structure used as a part of a turret punch press sheet positioning system. The objective is to find out the appropriate dimensional proportions for the linear axis frame to withstand the forces caused by the accelerations of the sheet movement. Determining factor is the maximum deflection of the frame and the resulting error in the sheet position at the punching center. In the literature research are presented the structural engineering theorems, which concern the three types of strain to which the frame structure is induced to: bending, shear and torsion. Formulas gathered from these theorems are then used for the deflection calculations. Resulting sheet movement at the punching center is assessed by a coordinate system transformation, where the vector components collected from the structural analysis are shifted from a local reference frame to a global coordinate system. Based on analytical calculations one frame candidate is selected for further analysis in FEM, which is used as a comparative method to examine the structural behaviour of the frame and to find out how the additional structural features effect the frame deformation. Results show that with the given load case, bending deflection is the dominant factor in the sheet displacement at the punching center, although the transverse displacement at the point of load doesn't translate as such in the positioning error: As the frame deflects, the cross-section also rotates according to the deflection curve, which causes the sheet to move in opposite direction to the load at the punching center, and therefore the positioning error is observed mainly in the longitudinal direction of the frame. The tested bracing methods increase mainly the torsional stiffness of the frame, and don't therefore have much effect on the positioning accuracy. According to results from FEM, the distortion of the frame cross-section due to asymmetrical force distribution isn't a major issue even in an unbraced construction as the transverse and torsional load partly cancel each other out.

# TIIVISTELMÄ

Lappeenrannan-Lahden teknillinen yliopisto LUT

LUT Energiajärjestelmät

Konetekniikka

Atte Anttila

## **Levytyökeskuksessa käytettävän lineaariakseliston rungon rakenteellinen mitoitus**

Diplomityö

2022

76 sivua, 44 kuvaa ja 18 taulukkoa

Tarkastajat: Professori Timo Björk

Diplomi-insinööri Jussi Kosola

Avainsanat: lujuusoppi, statiikka, elementtimenetelmä, teräsrakenteet

Tämän työn tutkimusaiheena on levytyökeskuksen levynpaikotusjärjestelmän osana toimivan hitsatun teräsrakenteen mitoitus. Tavoitteena on löytää lineaariakseliston rungolle sopivat mittasuhteet kantamaan levyn paikotuksesta aiheutuvat kiihtyvyydet. Määrittävänä tekijänä mitoituksessa on rungon joustamisesta aiheutuva levyn paikotusvirhe lävistyskeskiössä. Kirjallisuustutkimuksessa käydään läpi lujuusopin lausekkeet, jotka koskevat kolmea kuormitustyyppiä, joille runko altistuu: taivutus, leikkaus ja vääntö. Rungon siirtymät määritetään sen jälkeen kyseisiä lausekkeitä soveltaen. Rungon siirtymien aiheuttamaa levyn paikan muutosta lävistyskeskiössä arvioidaan koordinaatistomuunnoksen avulla, jossa siirtymälaskelmista kerätyt vektorikomponentit siirretään paikallisesta koordinaatistosta globaaliin koordinaatistoon. Analyyttisiin laskelmiin perustuen valitaan yksi runko vaihtoehto, joka viedään FEM-ohjelmistoon yksityiskohtaisempaa tutkimusta varten. FEMiä käytetään sekä analyttisten tulosten vertailukohtana, että määritettäessä rakenteeseen lisättävien piirteiden vaikutusta rungon siirtymiin. Tulokset osoittavat, että tutkimuksen kuormitustapauksessa rungon taipumalla on suurin vaikutus levyn siirtymään lävistyskeskiössä, vaikkei siirtymä kuormituspisteessä toistu sellaisenaan paikotusvirheenä: Rungon jostaessa, sen poikkileikkaus myös kiertyy taipumakäyrän mukaan, joka aiheuttaa levyn referenssipisteessä kuormitussuuntaan nähden vastakkaissuuntaisen siirtymän ja siten paikotusvirhe lävistyskeskiössä koostuu pääasiassa rungon pituussuuntaisesta komponentista. Rakenteessa testatut jäykisteratkaisut kasvattavat lähinnä vääntöjäykkyyttä, eivätkä siten vaikuta merkittävästi paikotustarkkuuteen. Epäsymmetrisestä kuormituksesta aiheutuva poikkileikkauksen vääristymä ei FEMin tulosten perusteella ole vaikutukseltaan kovin merkittävä edes jäykistämättömässä rakenteessa, koska poikittaisvoima ja vääntö kompensoivat toistensa vaikutuksen osittain.

## SYMBOLS AND ABBREVIATIONS

$\gamma$	Shear strain [rad]
$\varepsilon$	Normal strain [ $\Delta L/L_0$ ]
$\zeta$	Shear correction factor
$\kappa$	Curvature [ $1/R$ ]
$v(x)$	Bending deflection [mm]
$\sigma$	Normal stress [N/mm <sup>2</sup> ]
$\varphi$	Angle of twist [rad]
$\tau$	Shear stress [N/mm <sup>2</sup> ]
$a$	Torsional bending constant [mm]
$E$	Young's modulus [N/mm <sup>2</sup> ]
$F$	Force [N]
$G$	Shear modulus [N/mm <sup>2</sup> ]
$I$	Second moment of area [mm <sup>4</sup> ]
$I_p$	Polar moment of area [mm <sup>4</sup> ]
$I_v$	Torsion modulus [mm <sup>4</sup> ]
$I_w$	Warping constant [mm <sup>6</sup> ]
$L$	Length [mm]
$M$	Bending moment [Nm]
$R$	Radius of neutral axis [mm]
<b>R</b>	Rotation matrix
$r$	Radius of cross-section [mm]
$S$	First moment of area [mm <sup>3</sup> ]
$T$	Torque [Nm]
$w(x)$	Total deflection [mm]
$w_s(x)$	Shear deflection [mm]

## Table of contents

Abstract

Symbols and abbreviations

1	Introduction.....	6
2	Theoretical background for analytical methods.....	9
2.1	Transversely loaded beam - Euler-Bernoulli beam theory .....	9
2.2	Effect of shear in a transversely loaded beam .....	19
2.3	Structure under torsion.....	25
2.4	Distortion of a cross-section .....	36
2.5	Estimating sheet transition at the punching center .....	38
3	Results from analytical calculations .....	41
3.1	Model description .....	41
3.2	Transverse deflection and slope of the deflection curve.....	42
3.3	Deformation due to torsion .....	44
3.4	Sheet movement at the punching center .....	47
4	Results from FEM analysis.....	50
4.1	Deflection due to transverse force .....	50
4.2	Deformation due to torsion .....	52
4.3	Diagonal bracing against torsion .....	53
4.4	Refining the FEM model .....	55
4.4.1	Diagonal bracing.....	59
4.4.2	Diaphragm bracing .....	60
4.4.3	Effect of cut outs.....	63
4.4.4	Increasing the side wall thickness.....	66
5	Analysis of results.....	68
6	Conclusions.....	73
	References.....	75

# 1 Introduction

The research topic of this thesis is the structural engineering of a welded steel structure used as a part of a turret punch press sheet positioning system. The objective is to find out dimensional proportions for the frame structure to withstand the forces caused by the acceleration of the positioning system. Determining factor is the maximum deflection of the frame and the resulting error in the sheet position at the punching center. The dimensions and shape of the frame should be justified not only for minimum deflection, but also for efficient material usage. The scope of the thesis is defined to concern only the static analysis of the frame; dynamic analysis is limited out of the subject. The static analysis is further limited to concern only the deformation calculations of the frame, so the stress analysis isn't addressed in the thesis. Due to the high stiffness requirement of the frame though, the stresses will be quite mild overall, so the stress aspect is likely already met in the deformation based dimensioning.

Research questions of this thesis are:

- How the cross-sectional dimensions of the frame should be selected to withstand the forces caused by the accelerations of the positioning system?
  - Which are the main guidelines to design a structure:
    - Against bending
    - Against shear
    - Against torsion?
  - How these different types of deformations appear in achieving the target of precision at the punching center?
- How do the results obtained by FEM differ from the analytical ones, and does the FEM give some important information of the structure behaviour that an analytical approach doesn't?

To answer the questions, a literature research is first carried out to find out the basic concepts of the strength of materials to which the deflection calculations are based on. These concepts are then applied to form a proposal of the frame structure to best serve the load case. The

significance of the different types of deformations and the resulting error to the sheet position are assessed by a coordinate system transformation between local and global reference frame in 3D space. Finally, the FEM is used as a comparative method to determine the frame deflection and to get a more detailed results of the load case.

A simplified drawing of the sheet positioning system in a turret punch press is presented in Figure 1:

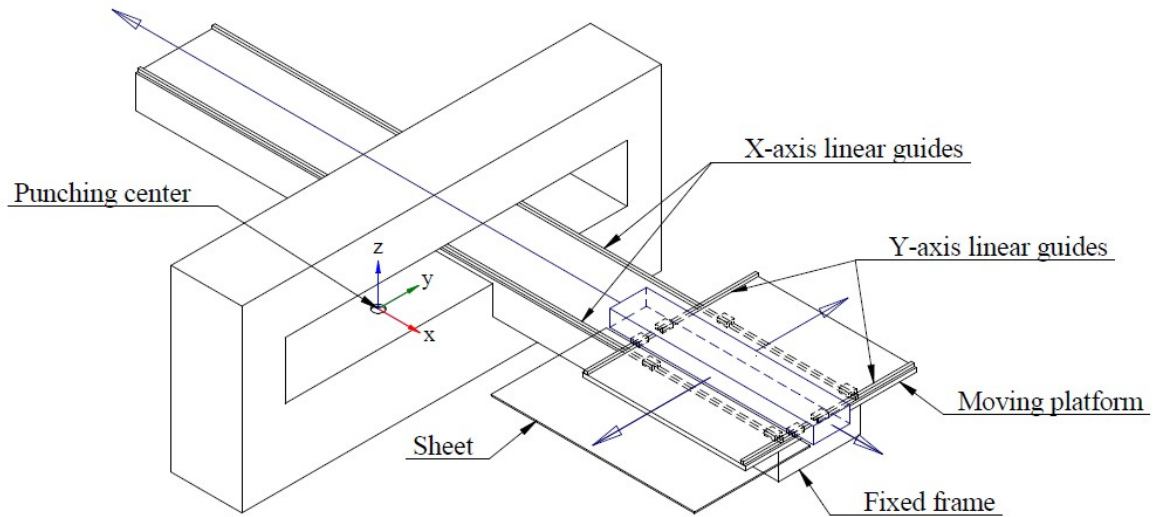


Figure 1. Turret punch press sheet positioning system

In the picture is shown a punching unit, which in this case is of a closed type (O-) frame, and the positioning system, which moves the sheet in a 2D coordinate system ( $x$ ,  $y$ ). The longest movement ( $x$ -axis) is built onto a fixed frame and the  $y$ -axis onto a moving platform. In this thesis the structure under investigation is the fixed frame, which is the largest single assembly in the positioning system and lays the basis for the rest of the system. At the punching center is marked the global origin of the system to which the position error of the sheet is later measured.

For structural analysis, a cantilever beam is selected as a boundary condition. The fixed frame is assumed to be rigidly supported by a perpendicular plane positioned to the axis of symmetry of the punching unit. Although the linear frame will be supported to the floor with

at least one foot per each side, they are left out of consideration to keep the focus only on the frame itself. The most critical load case is estimated to be the acceleration of the y-axis when the moving platform is driven to either end of the work area on the x-axis (frame free length at its maximum; 2150 mm). As the center of mass of the moving assembly is located some distance away from the fixed frame centroid, the acceleration will cause both transverse and torsion strain as shown in Figure 2 taken from the side:

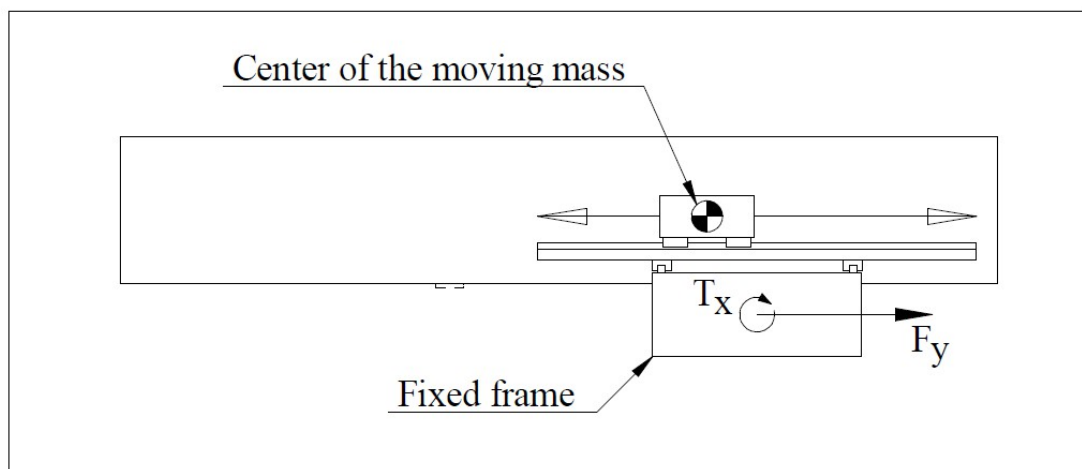


Figure 2. Side view of the positioning system

In the picture is shown the moving y-axis and its center of mass, which exact location is to be further defined during the design process. The acceleration of the y-slide causes transverse force  $F_y$  and moment  $T_x$  to the fixed frame. The bending, shear and torsion deflection of the frame should be very limited so that the sheet movement at the punching center stays within specified boundaries. Gravity isn't considered to have too significant role in the load case, so it is left out of consideration to focus only to the accelerations caused by the system itself.



## 2 Theoretical background for analytical methods

In the following are presented the structural engineering theorems, which concern the three types of strain to which the frame structure will be induced to: bending, shear and torsion. Formulas gathered from these theorems are later used for the analytical calculations of the frame deflection. The resulting sheet movement at the punching center is assessed by coordinate transformation where the vector components collected from the structural calculations are shifted from local reference frame to local coordinate system; the required work steps for this are also presented in this chapter.

### 2.1 Transversely loaded beam - Euler-Bernoulli beam theory

In structural mechanics the behaviour of a structure under transverse load is often visualized by investigating a beam element, where the transverse force induces a bending moment to the beam. To calculate deflections in such beam, formulas based on Euler-Bernoulli beam theory are used. The theory is also known as a classic beam theory or *engineer's beam theory*. It makes two simplifications to the problem: First assumption is that the beam is under pure bending so only the bending moment is considered and the cross-section planes of the beam will remain in plane during deflection, perpendicular to the beam axis. Second assumption is that the contours of the cross-section remain undeformed during bending. The first assumption neglects the effect of shear force, which in a beam subjected to a transverse load is also present in addition to the bending moment. The second assumption neglects the transverse shrinkage/swelling of the cross-section during bending. These two factors however, have typically very little impact on the magnitude of the total deformation on relatively long beams, yet involving them in the equations would make them much more complicated, so an assumption is made to leave them out of consideration in the theory. The Euler-Bernoulli assumptions enable straight forward geometric considerations of the problem as seen in Figure 3: (Outinen & Salmi 2004, p: 174 – 176.)

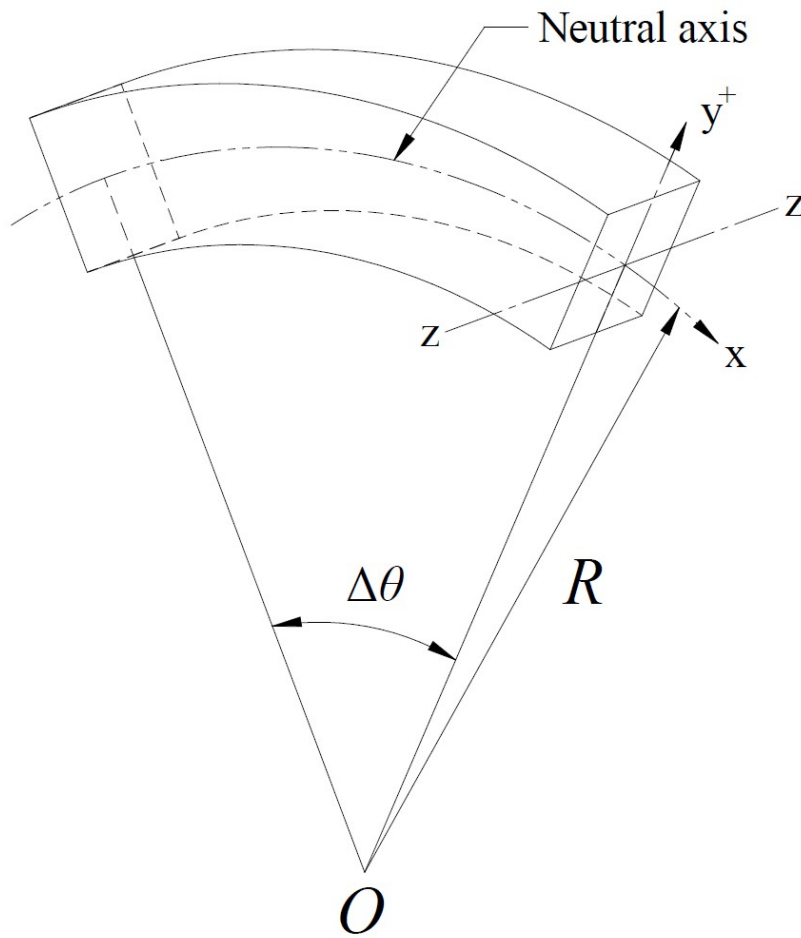


Figure 3. Euler-Bernoulli beam element (according to Parnes 2001, p. 245)

In the picture is presented a square bar element under pure bending. The point  $O$  marks the center of curvature;  $R$  the radius of the deformed neutral axis;  $\Delta\theta$  the angle between the element ends; and  $y$  the distance from the neutral axis. The element is subjected to a bending moment  $M$ , which is a constant along element length. Constant bending moment translates here to a constant bending radius. Since all the infinite thin cross-section slices, that build the square bar, are assumed to remain in plane also in deformed state, the resultant of the normal forces in the cross-section must be zero. In other words the normal forces above and below the neutral axis are equal but with opposite signs. This again means that the neutral axis must lie on the centroid of the cross-section as illustrated. These geometric assumptions lead to a situation, where the material “fibres” in the top surface must elongate and at the bottom surface compress when the element is bent downwards as illustrated. The normal strain  $\epsilon_x$  at an arbitrary height  $y$  can be calculated from the geometry: (Parnes 2001, p. 245 – 248.)

$$\begin{aligned}\varepsilon_x &= \frac{(R + y)\Delta\theta - R\Delta\theta}{R\Delta\theta} \\ \rightarrow \varepsilon_x &= \frac{y}{R}\end{aligned}\tag{1}$$

This change in fibre length (strain) is a percentile value ( $\Delta L/L_0$ ) and is proportional to the stress. According to Salmi & Pajunen (2010, p. 33) this stress-strain relation was first introduced by Jacob Bernoulli, and with ductile material like steel this relation is linear until the proportional limit of the material is reached. Until this limit the stress-strain curve follows equation known as *Hooke's law*:

$$\sigma_x = E\varepsilon_x\tag{2}$$

, where  $\sigma$  is the normal stress,  $E$  modulus of elasticity and  $\varepsilon$  strain. Parnes (2001, p. 134 – 135) notes that by definition, the proportional limit  $\sigma_p$  and elastic limit  $\sigma_e$  (Young's modulus) are different points but for steel and many other ductile materials, the difference between them is indistinguishable so that  $\sigma_p \approx \sigma_e$ . The two points are illustrated in Figure 4 below:

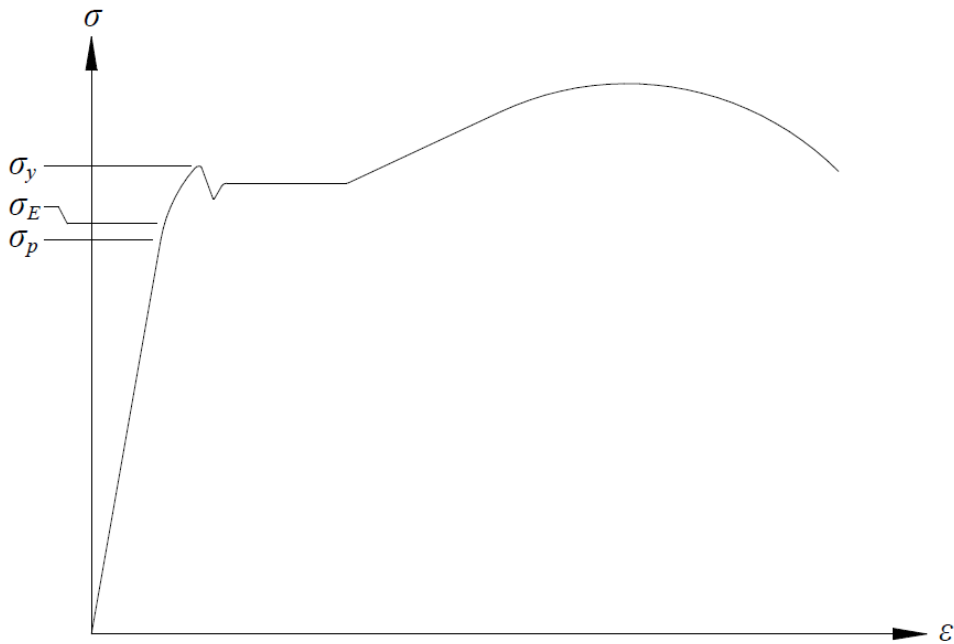


Figure 4. Stress-strain curve for low-carbon steel (according to Salmi & Pajunen 2010, p. 35)

In the picture is shown a typical stress-strain curve for low-carbon steel. The elastic limit locates slightly higher than the proportional limit. By combining the Bernoulli strain equation (1) and Hooke's law (2), the stress in arbitrary height in the cross-section can be obtained as:

$$\sigma_x = \frac{Ey}{R} \quad (3)$$

From the equation can be noted that the stress varies linearly with the perpendicular distance from the neutral axis: This follows the Euler-Bernoulli assumption that cross-sections will remain in plane. The stress  $\sigma_x$  is referred here as *bending stress*. The bending moment  $M$  can be considered as a sum of the normal forces acting on infinite small areas  $dA$ , dependent of the distance  $y$  so that:

$$\begin{aligned} M &= \iint y \sigma_x dA \\ \text{by substituting } \rightarrow \sigma_x &= \frac{Ey}{R} \\ M &= \iint y \left( \frac{Ey}{R} \right) dA \\ M &= \frac{E}{R} \iint y^2 dA \end{aligned} \quad (4)$$

In the equation the double integral  $y^2 dA$  is the second moment of cross-sectional area about the neutral axis ( $z - z$ ) and is commonly designated with  $I$ . Placing this to the equation, the moment-curvature relation is simplified to:

$$M = \frac{EI}{R} \quad (5)$$

, which is known as the *Euler-Bernoulli relation*. The numerator  $EI$  is called flexural rigidity and depends on material stiffness  $E$ , and the second moment of cross-sectional area  $I$ , which is a geometric property. The equation can also be written in a form, which is later used to determine the curvature of the deformed beam:

$$M = EI\kappa \quad (6)$$

, where  $\kappa$  is the curvature ( $1/R$ ) of the deflection curve. (Parnes 2001, p. 247.)

Although by definition, the Euler-Bernoulli relation concerns only beams in pure bending, it is also used to determine flexure of beams induced to transverse load acting in vertical plane, so that  $M$  is no longer constant but a linear function of distance  $x$  as in the picture below. In this situation, the plane sections of the beam don't rigorously follow the Euler-Bernoulli assumption, which is that the plane sections remain in plane also in deformed state. However, the warping effect is so small in relatively long beams that an assumption is made that even in these conditions the plane sections will remain in plane, perpendicular to the deformed neutral axis. This assumption is known as *Navier's hypothesis* and equations used accordingly are known as engineering beam formulas, which provide very accurate solutions to a wide variety of engineering problems. (Parnes 2001, p. 255 – 256.)

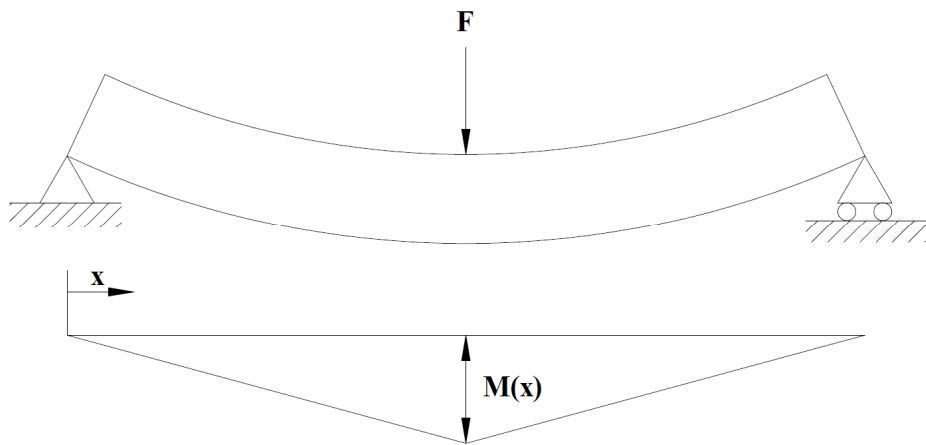


Figure 5. Beam under transverse load and the moment diagram (according to Valtanen 2019, p. 316)

In Figure 5 is shown an example of a transversely loaded beam and its moment diagram. To solve for the curvature  $\kappa$  of the deflection curve, an equation known from calculus is used, which gives the curvature of any curve lying in a 2-dimensional coordinate system when the necessary boundary conditions are known (Parnes 2001, p. 314):

$$|\kappa(x)| \equiv \frac{1}{R(x)} = \left| \frac{\frac{d^2 v(x)}{dx^2}}{\left\{ 1 + \left[ \frac{dv(x)}{dx} \right]^2 \right\}^{\frac{2}{3}}} \right| \quad (7)$$

, where  $v(x)$  is the deflection curve. By choosing positive curvature  $\kappa > 0$  so that the point  $O$  (vertex point of the angle  $\theta$ ) will lie on positive  $y$  side, and substituting this to the Euler-Bernoulli relation gives:

$$\begin{aligned} EI\kappa(x) &\equiv -EI \left| \frac{\frac{d^2 v(x)}{dx^2}}{\left\{ 1 + \left[ \frac{dv(x)}{dx} \right]^2 \right\}^{\frac{2}{3}}} \right| = M(x) \\ \Rightarrow EI \frac{d^2 v(x)}{dx^2} &= - \left\{ 1 + \left[ \frac{dv(x)}{dx} \right]^2 \right\}^{\frac{2}{3}} M(x) \end{aligned} \quad (8)$$

By assuming that the beam has a relatively high flexural rigidity (i.e. deflection is small compared to the span length so that the slope of the deformed beam  $[dv(x)/dx] \ll 1$ ), the equation can be reduced to:

$$EI \frac{d^2 v(x)}{dx^2} = -M(x) \quad (9)$$

With this equation, the deflection of the beam can be calculated by solving for the curve  $v(x)$ . The solution of the problem requires integration of the equation and determination of the boundary conditions which depend on the beam supporting. These boundary conditions provide the two integration constants needed. (Parnes 2001, p. 315.)

In the following the boundary conditions and the resulting formulas for deflection curve are determined for a cantilever beam (Salmi & Pajunen 2019, p. 209):

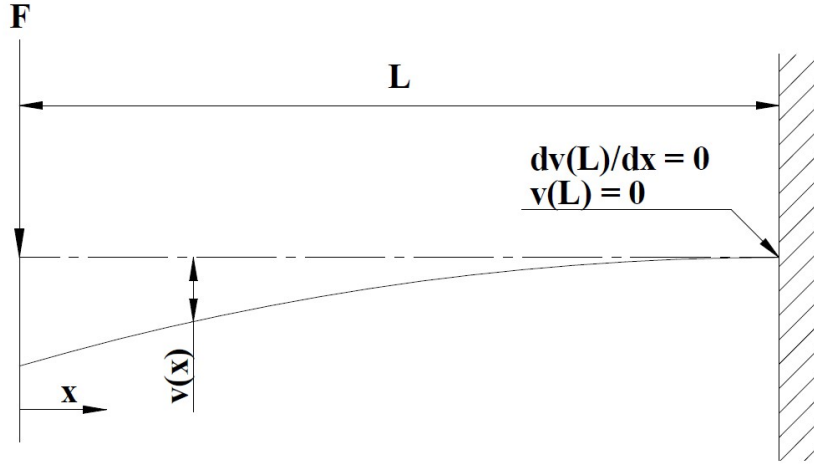


Figure 6. Deflection curve of a cantilever beam (according to Salmi & Pajunen 2019, p. 209)

In Figure 6 is shown a cantilever beam with a tip load  $F$  acting on the free end. The continuous line marks the deflection curve  $v(x)$ . To the fixed end is marked the two resulting boundary conditions: Both the magnitude of the deflection and the slope of the deflection curve have to be zero. In this case the origin ( $x = 0$ ) is placed at the free end of the beam so that:

$$EI \frac{d^2 v(x)}{dx^2} = -M(x) = Fx \quad (10)$$

By integrating the deflection equation twice, one first gets:

$$EI \frac{dv(x)}{dx} = \frac{1}{2} Fx^2 + C_1$$

and after second integration:

$$EIv(x) = \frac{1}{6} Fx^3 + C_1x + C_2 \quad (11)$$

, where  $C_1$  and  $C_2$  are integration constants. Their values can be obtained based on the boundary conditions. In this case the boundary conditions determine that the slope at the fixed end must be zero as in picture, so that:

$$\frac{dv(L)}{dx} = 0$$

, which leads to:

$$\Rightarrow \frac{1}{2}FL^2 + C_1 = 0$$

$$\Rightarrow C_1 = 0$$

Similarly, the magnitude of the deflection at the root must be zero:

$$v(L) = 0$$

$$\Rightarrow \frac{1}{6}FL^3 + C_1L + C_2 = 0$$

$$\Rightarrow C_2 = -\frac{1}{6}FL^3$$

When these constants are placed on the deflection equations, the final result is obtained as (Salmi & Pajunen 2019, p. 209):

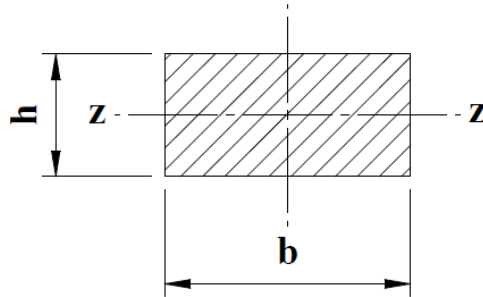
$$v(x) = \frac{FL^3}{6EI} \left[ 2 - 3\frac{x}{L} + \left(\frac{x}{L}\right)^3 \right] \rightarrow v(0) = \frac{FL^3}{3EI} \quad (12)$$

$$\frac{dv(x)}{dx} = \frac{FL^2}{2EI} \left[ 1 - \left(\frac{x}{L}\right)^2 \right] \rightarrow \frac{dv(0)}{dx} = \frac{FL^2}{2EI} \quad (13)$$

These equations, among others, for selected problems of differently supported and loaded beams can be found in structural engineering literature, where they are listed in tables, like Valtanen (2019, p. 316 – 329). When examining the deflection equations not only for a cantilever beam, but for other transversely loaded beams as well, the magnitude of the deflection is found to be inversely proportional to the flexural stiffness,  $EI$ . This relation is found to be true for any beam governed by the Euler-Bernoulli relations (Parnes 2001, p. 321). For great bending stiffness, either one or both of the mentioned values ( $E$  and  $I$ ) should be maximized. As the  $E$  is a material property it is “locked in” after the material has been selected, but the second moment of cross-sectional area ( $I$ ) can be greatly affected by design. To calculate the second moment of area of a cross-section, one may refer to the tables found in structural design handbooks, where formulas for a variety of different cross-sections are



presented. For example, the second moment of area for a solid rectangular section (Figure 7) is given as (Valtanen 2019, p. 305):



$$I_{z-z} = \frac{bh^3}{12} \quad (14)$$

Figure 7. Second moment of area for a rectangular cross-section (according to Valtanen 2019, p. 305)

The formula above shows, that the height ( $h$ ) of the section against the neutral axis is the dominant factor as it is raised to the third power. This is consistent with the previously presented bending theory, where the material furthest away from the neutral axis carries the most of the load as stated in eq. 3 (page 12). Material located near the neutral axis contributes very little to the load carrying capacity of the beam as the normal stress closes zero towards the neutral axis. For efficient design the material should be moved as far away as possible from the neutral axis to contribute the best to the bending stiffness. To calculate the second moment of area for an element placed some distance away from the neutral axis, a method called *parallel axis theorem* is used. The theorem is also known as Steiner's theorem or Steiner's rule. It adds the moment distance of the cross-sectional area to the equation (Salmi & Pajunen 2010, p. 424):

$$I_{z-z} = I_{z'-z'} + Ay^2 \quad (15)$$

, where  $I_{z'-z'}$  is the second moment of area of the cross-section around its own centroid axis,  $A$  is area of the cross-section and  $y$  is the distance from the neutral axis to the cross-section centroid. In the following is presented the significance of the distance from the neutral axis to the location where the material is placed:

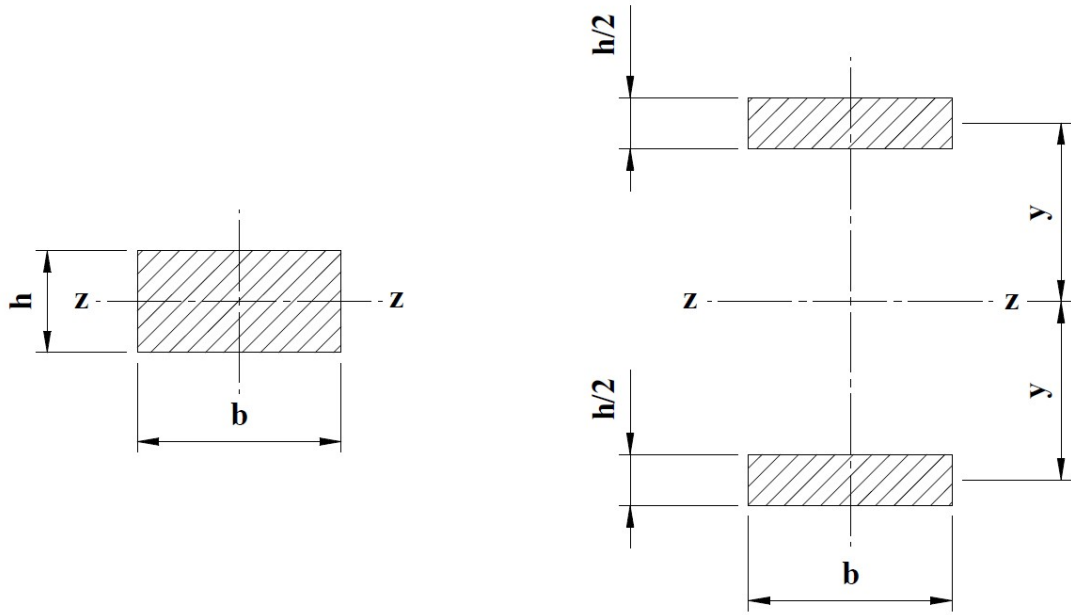


Figure 8. Rectangular section and idealized section (according to Bauchau & Craig 2009, p. 195)

In Figure 8 are shown two cross-sections both with the same cross-sectional area, but one being a solid rectangle placed concentrically with the neutral axis and the other one being an “idealized” section. The ratio of the bending stiffness between the two can be denoted as: (Bauchau & Craig 2009, p. 195)

$$\frac{I_{idealized}}{I_{rectangle}} = \frac{2 \left[ \frac{b(h/2)^3}{12} + \frac{bh}{2} y^2 \right]}{\frac{bh^3}{12}} = \frac{1}{4} + 12 \left( \frac{y}{h} \right)^2 \quad (16)$$

The result is the ratio of the second moment of areas between the two. It can be seen that the ratio rises exponentially in favour of idealized section, and already with  $y/h = 2$  the idealized section has approximately 48 times greater bending stiffness. In practice the ideal section obviously needs a web to connect the two flanges together as is the case in an I-beam, but this shows that the rational design of a transversely loaded beam calls for maximum height. The limiting factor in the section height is the instability, which with extreme dimensions may become an issue in the form of lateral-torsional buckling tendency (Bauchau & Craig 2009, p. 196).

## 2.2 Effect of shear in a transversely loaded beam

With relatively long beams the magnitude of shear deformation compared to the deformation caused by the bending moment is so miniscule that it can usually be neglected, but as the length of the beam compared to its height gets really short, the influence of shear deformation may become so significant that it has to be taken into consideration. Figure 9 presents a simplified drawing of shear deformation on a cantilever beam:

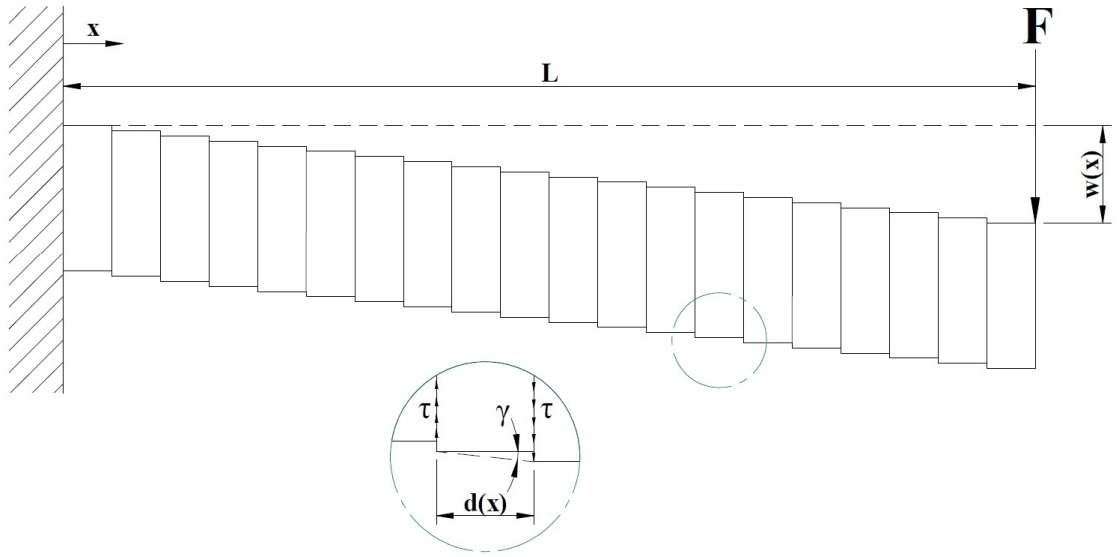


Figure 9. Deflection of a cantilever beam due to shear (according to Blodgett 1972, p. 2.6-2)

In the picture a beam with length  $L$  is loaded with a transverse force  $F$ , which causes shear stress  $\tau$  and shear deflection  $w(x)$ . The average shear strain  $\gamma$  is determined by dividing the shear force with shear modulus  $G$  and shear area  $A$ :

$$\gamma_{avg} = \frac{F}{GA} \quad (17)$$

The result is the angle  $\gamma$  in radians as shown in detail. The expression *average shear strain* is to be noted, as the distribution of shear stress and shear strain in reality varies strongly across the cross-section depending on the geometry. As the stress varies across the cross-

section, so will the cross-section planes warp (will not remain in plane) and the strain  $\gamma$  varies correspondingly across the height of the cross-section as shown on the right in Figure 10:

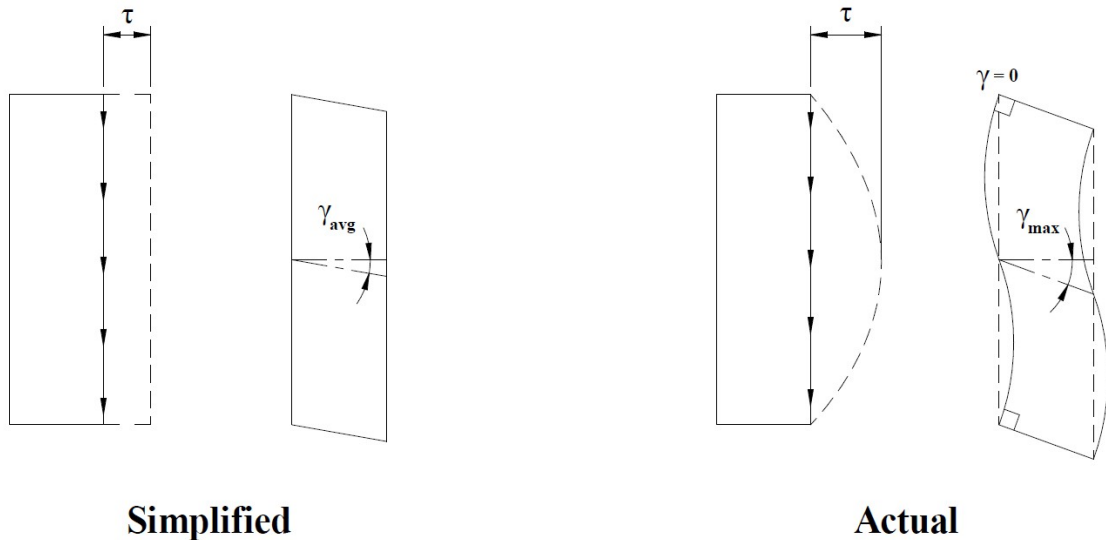


Figure 10. Simplified and actual shear deformation (according to Bauchau & Craig 2009, p. 798)

On the left is shown the average shear stress distribution and on the right the actual distribution on a rectangular cross-section. On the simplified model, the shear stress is a constant ( $F/A$ ) even in free surfaces, which is incorrect as on free surface there can't be any shear force present. In the actual distribution the shear stress on the free surfaces is zero ( $\tau = 0 \rightarrow \gamma = 0$ ) and the distribution along the cross-section height has a parabolic shape as shown in the picture. (Bauchau & Craig 2009, p. 798.)

With more complex shapes the unevenness of the shear stress distribution is even more notable, like in an I-beam shown in Figure 11:

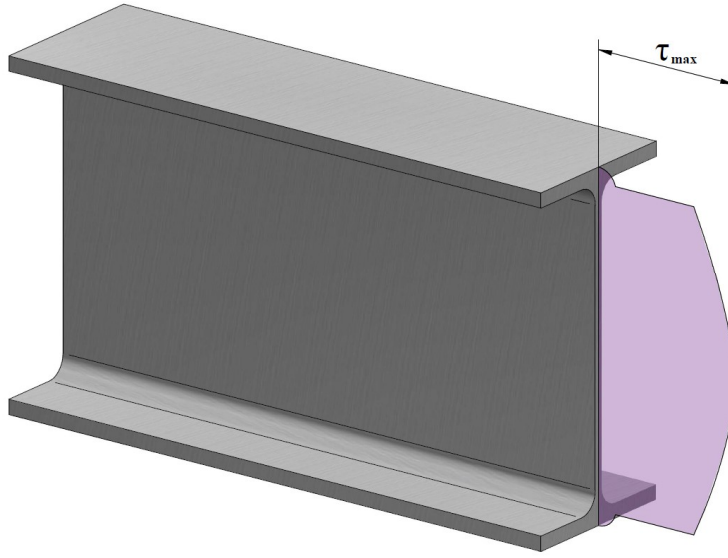


Figure 11. Shear stress distribution in an I-beam centroid plane (according to Singh 2021, p. 233)

In an I-beam the vertical shear stress is carried almost entirely by the web plate as shown in the picture taken from the centroid plane. The shear stress distribution curve has a parabolic shape between break points and reaches its peak ( $\tau_{max}$ ) at the centroid. In order to calculate shear deflection at the neutral axis, one has first obtain the shear stress at this point by using the shear formula (Gere & Goodno 2012, p. 322):

$$\tau_{max} = \frac{FS}{It} \quad (18)$$

, where  $S$  is the first moment of area above the point investigated, taken around the neutral axis,  $I$  the second moment of area of the entire cross-section (around the neutral axis) and  $t$  the thickness of the web plate. From here can be obtained a constant known as *form factor*, or *shear correction factor*, which is designated here with  $\zeta$ . It is the ratio between the maximum shear stress and the average shear stress (Blodgett 1972, p. 2.6-2):

$$\zeta = \frac{\tau_{max}}{\tau_{avg}} = \frac{\left(\frac{FS}{It}\right)}{\left(\frac{F}{A}\right)} = \frac{AS}{It} \quad (19)$$

The first moment of area can be denoted as (Gere & Goodno 2012, p. 328):

$$S = \int y dA \quad (20)$$

, which also has a form:

$$S = \sum y_i A_i \quad (21)$$

, where  $y$  is the distance measured from the centroid of an area to the neutral axis as shown in Figure 12:

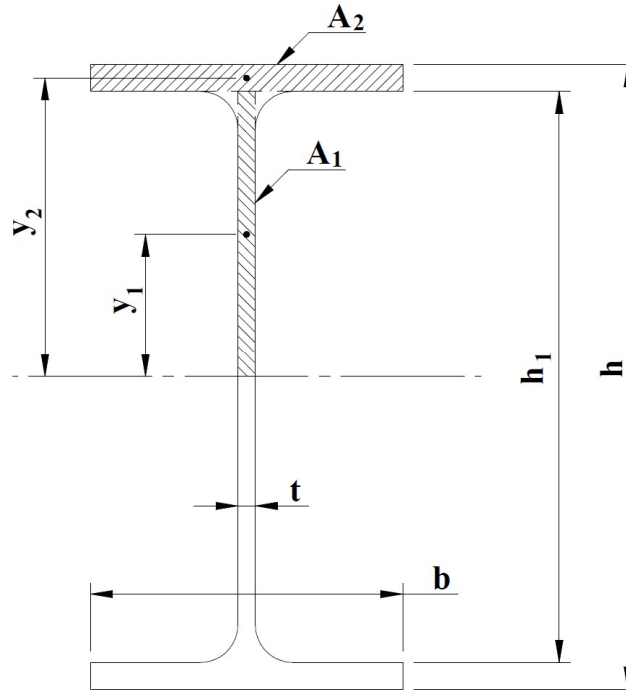


Figure 12. First moment of area above the neutral axis of an I-beam (according to Gere & Goodno 2012, p. 324)

The corner fillets are neglected so the first moment of area for an I-beam can be calculated from the dimensions marked in the picture as (Gere & Goodno 2012, p. 324):

$$S = \frac{1}{8}(bh^2 - bh_1^2 + th_1^2) \quad (22)$$

, where  $b$  is the width of the flange,  $h$  the overall height of the beam and  $h_1$  the height of the web. According to Blodgett (1972, p. 2.6-3) the formula can be used also for a box section as shown in Figure 13:

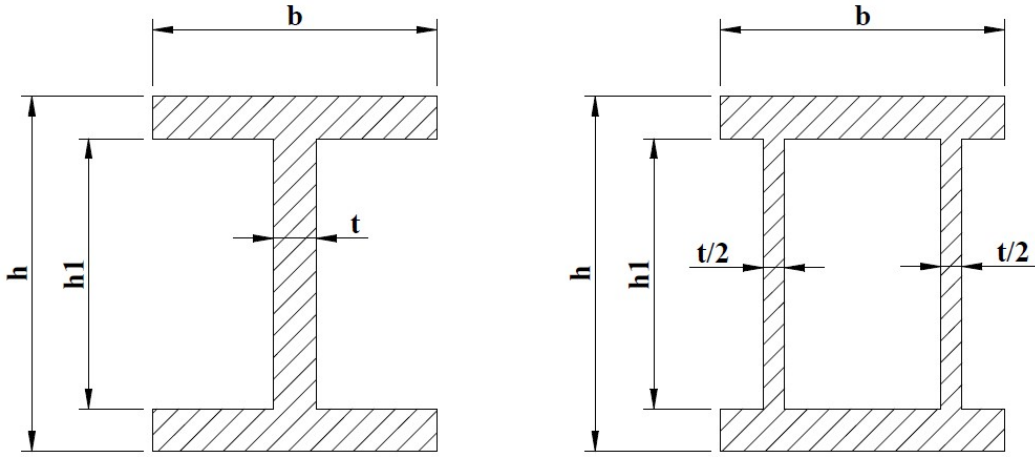


Figure 13. Beam sections with identical first moment of area and shear correction factor (in vertical direction) (according to Blodgett 1972, p. 2.6-3)

By applying the equation of the first moment of area  $S$  to the formula, the shear correction factor  $\zeta$  can be denoted as:

$$\zeta = \frac{A}{8It} (bh^2 - bh_1^2 + th_1^2) \quad (23)$$

Resulting value is the factor with which the shear force  $F$  must be multiplied to obtain the shear strain at the centroid (Pennala 2002, p. 128):

$$\gamma_{max} = \frac{F\zeta}{GA} \quad (24)$$

As the angle  $\gamma$  is very small, it can be written that the angle approximately equals with the slope of the deflection curve of the beam so that the actual shear deflection can finally be obtained by:

$$\gamma \cong w'_s(x) = \frac{F\zeta}{GA} \quad (25)$$

and after integration:

$$\rightarrow w_s(x) = \frac{F\zeta}{GA} x + C \quad (26)$$

Applying the boundary conditions  $w_s(L) = 0$  leads to  $C = 0$ , and thus:

$$w_s(L) = \frac{FL\zeta}{GA} \quad (27)$$

In some literature concerning the subject (e.g. Gross. et.al. 2011) a correction factor is used in the equation *below* the division sign as a factor for the shear area and has therefore inverse values. It is also a common practice to use an approximation value for the shear corrected area assuming that the web takes all the shear stress so that  $A_{shear} = A_{web}$ . With typical proportions of a double flanged standard beams this is pretty accurate as the web carries 90% to 98% of the total shear stress (Gere & Goodno 2012, p. 325).

By combining the flexure due to the bending moment (Euler-Bernoulli beam) and the shear force, the total flexure of the beam can be obtained as (Gross et.al. 2011, p. 161 – 162):

$$\begin{aligned} w(L) &= w_B + w_s \\ \rightarrow w(L) &= \frac{FL^3}{3EI} + \frac{FL\zeta}{GA} \end{aligned} \quad (28)$$

, where the first term  $w_B$  is the flexure according to the Euler-Bernoulli beam and  $w_s$  the flexure due to shear. Evaluating the effect of shear in the total deformation, the equation may be arranged to the form (Gross et.al. 2011, p. 162):

$$w(L) = \frac{FL^3}{3EI} \left( 1 + \frac{3EI\zeta}{GAL^2} \right) \quad (29)$$

, where the term inside the brackets represents the influence of shear. From the equation can be observed that the geometric properties length ( $L$ ) and the second moment of area ( $I$ ) are placed on opposite sides of the division line between the two terms. This is consistent with the assumption, that the longer the beam gets compared to the flexural stiffness, the greater the proportion of bending deflection compared to shear deformation becomes. In Figure 14 is shown an example of the shear and bending deformation ratio on a tip loaded IPE200 cantilever beam:



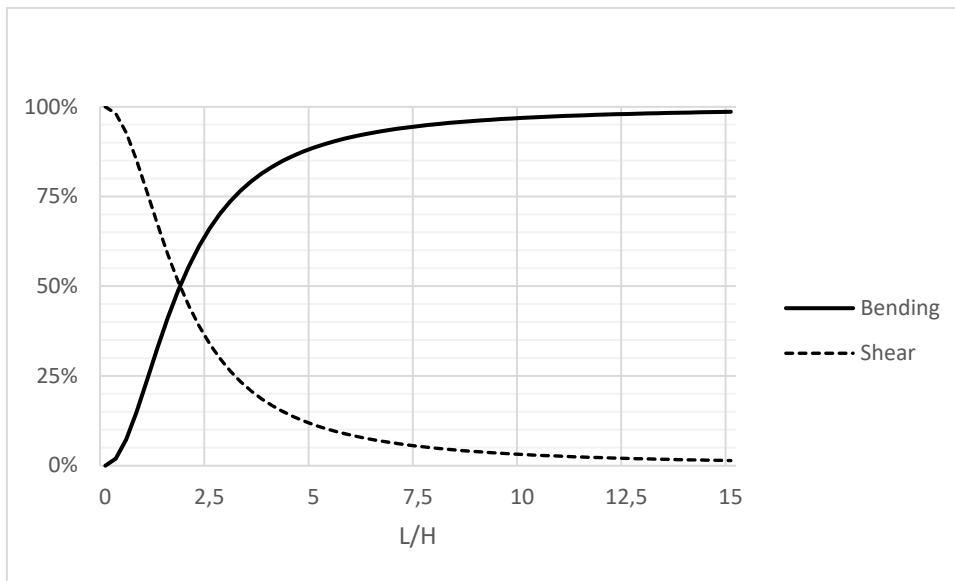


Figure 14. Ratio of shear and bending deformation on IPE200 cantilever with tip load

From the graph can be seen the rapid change from shear to bending deflection with the increase of the length of the beam. For  $L/H = 7.5$  the bending deformation accounts already close to 95% of the total deformation. Likewise, if the web thickness of the beam would be increased, the intersection of the two graphs would be located even more to the left, as the balance between shear stiffness vs. bending stiffness would change more in favour of shear stiffness (= smaller shear deformation).

### 2.3 Structure under torsion

Basic relations for torsion deflection can be deduced by investigating a cylindrical cantilever rod with a torque  $T$  acting on the free end (Figure 15):

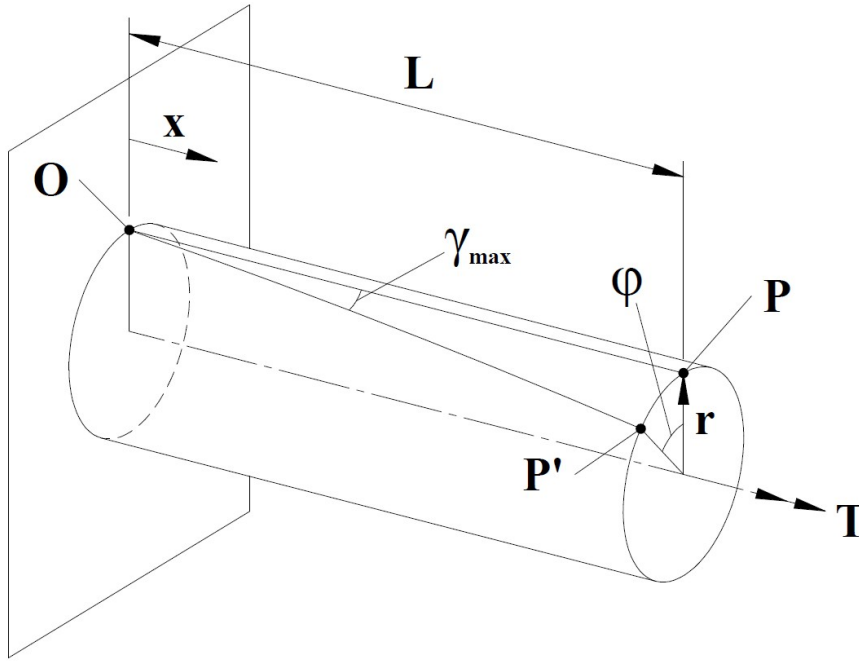


Figure 15. Cylindrical rod under torsion (according to Da Silva 2006, p. 350)

The torque causes the face of the rod to turn counter clockwise and this change in the angle of twist is marked with  $\phi$  (radians) and it is a function of distance  $x$ . The shear strain caused by the torque is marked with  $\gamma$  (radians) and it is a function of radius  $r$  as it is established in the following equations. The polar coordinate  $P$  marks a position on the cylinder surface before the deformation and point  $P'$  the location of the same point after the displacement. Point  $O$  is placed on the same polar coordinate as  $P$ , but to the fixed end, so it stays in place during deformation. In the case of small deformations, the distances  $\overline{OP}$  and  $\overline{OP'}$  may be considered as equal, so the distance  $\overline{PP'}$  can be expressed in two ways: (Da Silva 2006, p. 350.)

$$\begin{aligned}\overline{PP'} &= r d\phi \cong \gamma dx \\ \Rightarrow \gamma &= r \frac{d\phi}{dx}\end{aligned}\tag{30}$$

, where the term  $d\phi/dx$  is the *angle of twist per unit length*. For simplification it may be marked with  $\theta$ , so that:

$$\gamma = r\theta\tag{31}$$

For linear elastic material the shearing stress is proportional to the strain (Hooke's law):

$$\tau = G\gamma = Gr\theta \quad (32)$$

As the shear stress is proportional to the radial distance from the axis of twist so must be the resisting moment in a cross-section be incremental but also equal to the applied torque  $T$ . The incremental moment about the axis of twist due to the shear stress acting on an element  $dA$  at a distance  $r$  can be defined as (Parnes 2001, p. 194):

$$\begin{aligned} \Delta T &= r\tau dA \\ \rightarrow \text{substituting } \tau &= Gr\theta \\ \Delta T &= Gr^2\theta dA \end{aligned}$$

Therefore, the total moment acting on a cross-section is given by:

$$T = G\theta \iint r^2 dA \quad (33)$$

The integral is recognised as the polar moment of area about the axis of twist and can be designated with  $I_p$  so that:

$$\theta = \frac{T}{GI_p}$$

Finally, the angular deflection for an element of length  $L$  is:

$$\Delta\varphi = \frac{TL}{GI_p} \quad (34)$$

Being first derived by Charles Coulomb in 1784, the above is known as Coulomb torsion solution (Parnes 2001, p. 197). It gives the result for the angle of twist in radians and is valid *only* for members of a circular shape (rod or tube). For members of an arbitrary shaped cross-section, the polar moment of area is replaced with a more common *torsion modulus*,  $I_v$ . The full derivation of the formulas used to calculate the torsion modulus for different kinds of cross-sections will not be covered here as some of them are quite complex yet they still are only approximations since there isn't an easy, all-inclusive method to determine the shear stress distribution exactly for an arbitrary shaped cross-section. The research to which the

formulas are based when determining the torsion modulus of a cross-section include Saint-Venant 1855 (thick solid sections), Föppl 1921 (thin-walled open sections), Bredt 1896 (thin-walled closed sections) and Prandtl 1903 (membrane analogy for the shear stress distribution) (Salmi & Pajunen 2010, p. 239 – 263). From the names mentioned, *Saint-Venant torsion* is commonly used term to designate the theory of pure torsion in a broad sense (Hughes et.al 2011, p. 7).

As mentioned, the shear stress is proportional to the radial distance  $r$  from the axis of twist. With a circular member, the distribution is also linear and applies both to a solid and a hollow circular shaft, as shown in Figure 16 below:

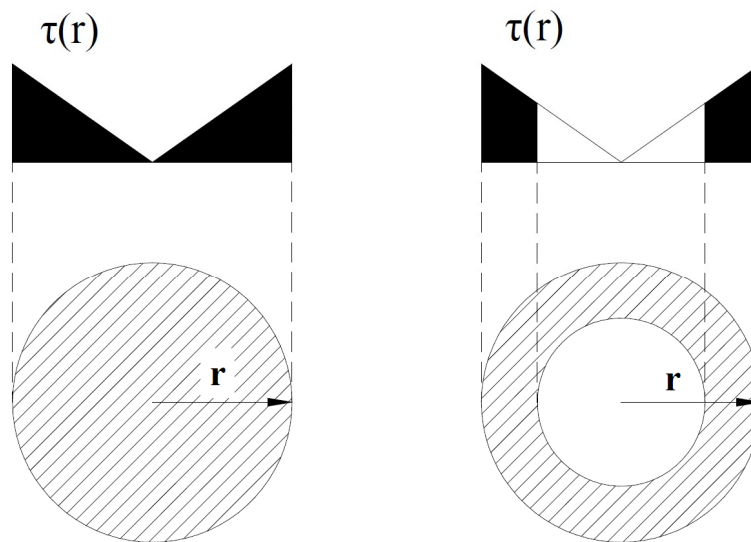


Figure 16. Shear stress distribution on a solid and a hollow circular shaft (according to Pennala 2002, p. 194 – 196)

As seen in the picture, the magnitude of the shear stress ( $\tau$ ) varies linearly along the radial distance and closes zero towards the central region, which contribution to the overall torsional rigidity is very little compared to the outer region. Therefore, if material saving is important, a hollow shaft is preferred. With a hollow shaft it must be ensured though, that the wall thickness is sufficient enough to avoid stability issues (Parnes 2001, p. 205). In practical applications there is almost always other stress types present in addition to torsion. For example, bending vibration is usually present to some degree in power transmission

applications and should therefore be considered when determining the minimum wall thickness (Karhunen et.al. 2012, p. 187 – 191).

When designing a torsion resistant structure, Blodgett 1972 (p. 2.10-1) lists three basic rules to follow:

1. Closed sections are used where possible
2. Diagonal bracing (in built-up frames)
3. Rigid end connections

The influence of the first item on the list can be illustrated by comparing the torsional modulus of the two otherwise similar square hollow sections, but one being closed and the other one open (Figure 17):

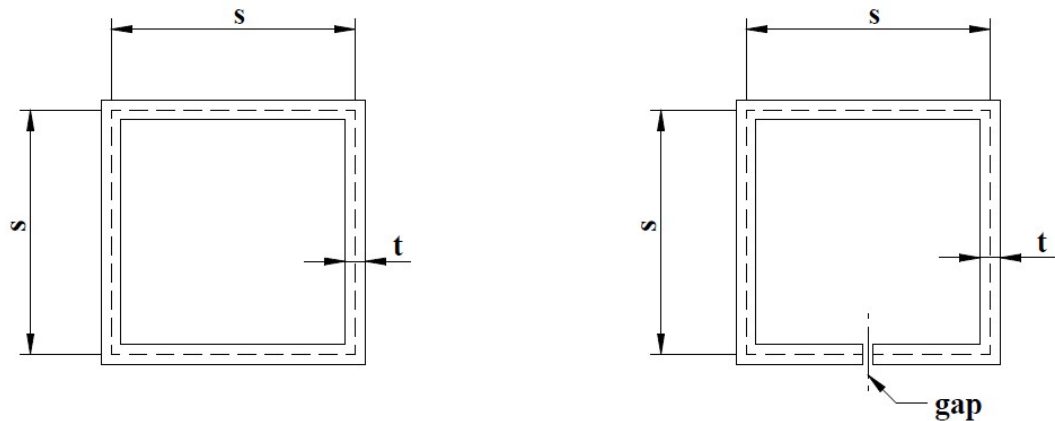


Figure 17. A closed and an open square hollow section

The sections have uniform wall thickness and for the open section the gap is assumed to be infinite narrow to simplify the dimensions for the calculation. For the closed section, the formula derived from Bredt's analysis can be used to determine the torsion modulus  $I_v$  (Salmi & Pajunen 2010, p. 257):

$$I_v = \frac{4\bar{A}^2}{\sum \left( \frac{s_i}{t_i} \right)} \quad (35)$$

, where  $\bar{A}$  is the area enclosed by the center line,  $s$  is the edge length and  $t$  is the wall thickness as illustrated. As the example sections have only walls of single thickness and length, the equation may be simplified to:

$$\begin{aligned} I_v &= \frac{4(s^2)^2}{\frac{4s}{t}} \\ \Rightarrow I_v &= \frac{s^3}{t^{-1}} \end{aligned} \quad (36)$$

The open section uses different formula to obtain the torsion modulus. According to Föpl's formula (Karhunen et.al.2012, p. 217) the torsion modulus is:

$$I_v = \frac{1}{3} \sum s_i t_i^3 \quad (37)$$

, and for a section with square dimension and uniform wall thickness:

$$\Rightarrow I_v = \frac{4st^3}{3} \quad (38)$$

From here the impact between closed vs. open section to the torsional rigidity can be illustrated by looking at the ratio of the torsion modules between the two:

$$\frac{I_{v_{closed}}}{I_{v_{open}}} = \frac{\left(\frac{s^3}{t^{-1}}\right)}{\left(\frac{4st^3}{3}\right)} = \frac{s^3 t}{\frac{4}{3} st^3} = \frac{s^2}{\frac{4}{3} t^2} \quad (39)$$

With example dimensions of  $s = 250$  and  $t = 20$  the torsions modulus of a closed section is already 117 times better than in the open section. This is due to the significant difference in the shear stress distribution and the shear flow between the two. With closed section the shear flow can run on one direction around the circumference of the section whereas in open section it must run in two directions and the shear stress change to its opposite value across the thickness of the section (Salmi & Pajunen 2010, p. 262).

According to Karhunen et.al. 2012 (p. 218) Föppl's formula usually gives a bit too small values for the torsion modulus. To increase precision, a correction factor can be used which is dependent of the cross-section type so that:

$$I_v = \frac{\eta}{3} \sum s_i t_i^3 \quad (40)$$

, where  $\eta$  varies from around 1 to 1.3 between L-, C-, T-, I and H-beams accordingly. Values can be found from structural engineering literature; for example Valtanen 2019 (p. 362). However, using the correction factor has still very little improvement to the torsion modulus compared to a closed section, and Karhunen et.al. (2012, p. 215) mentions consequently, that by adding more bends to an open cross-section one won't get a significant improvement on the torsional rigidity.

The second item in the Blodgett's list, diagonal bracing, is based on a knowledge that a member under torsional loading produces both transverse shear stresses and longitudinal shear stresses, and that these stresses combined produce a diagonal tensile and compressive stresses which are maximum at 45 degree angle; this is illustrated in Figure 18. (Blodgett 1972, p. 2.10-17.)

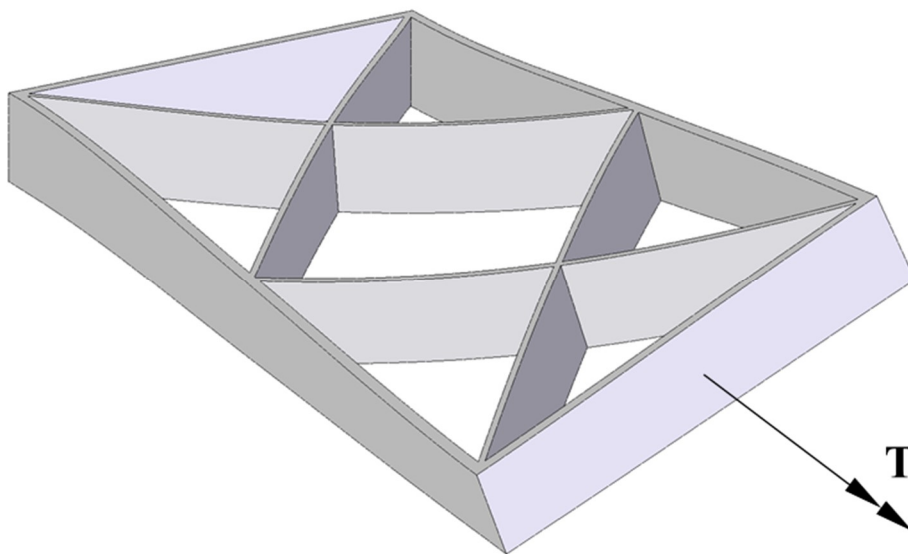


Figure 18. Double diagonal bracing on a built-up frame (according to Blodgett 1972, p. 2.10-17)

In the picture is shown a built-up frame with double diagonal bracing. When torque is applied, the diagonal supports bare the tensile and compressive stresses caused by the torsion. As the transverse and longitudinal shear components cancel each other out, there is no twisting action on a diagonal member placed at 45 degree to the frame as shown. (Blodgett 1972, p. 2.10-17.)

The last item in Blodgett's list, rigid end connections, concerns the warping restriction of a cross-section under torsion (Blodgett 1972, p. 2.10-21). By restricting the torsional warping of a cross-section, it is possible to improve the torsional behaviour (decrease the angle of twist) especially in double flanged sections. In Figure 19 is shown an I-beam, which is prone to warping in unrestricted torsion:

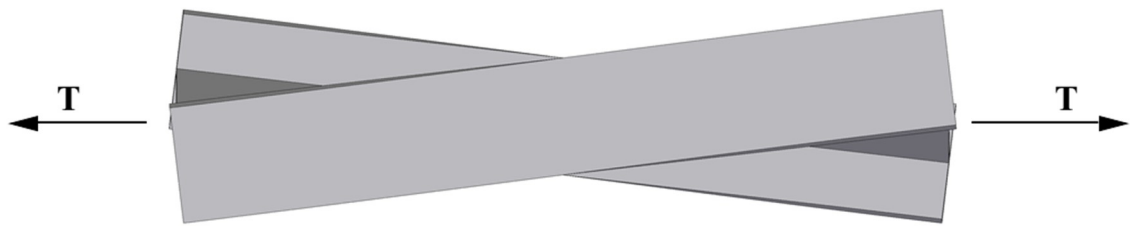


Figure 19. Free warping of an I-beam (according to Hughes et.al 2011, p. 8)

In the picture an I-beam is loaded by a torsion couple as shown – no additional supporting is present. From the picture can be seen, that the cross-sections no longer remain in plane, perpendicular to the longitudinal axis, but that the upper and lower flanges rotate to their opposite directions as seen from the top view. This counter rotation, known as warping, is characteristic behaviour to open, double flanged sections such as I-beams (Hughes et.al. 2011, p. 8). In the picture is also notable that the top and bottom flanges themselves stay relatively straight.

Figure 20 shows the same beam, but now with a rigid connection at one end:



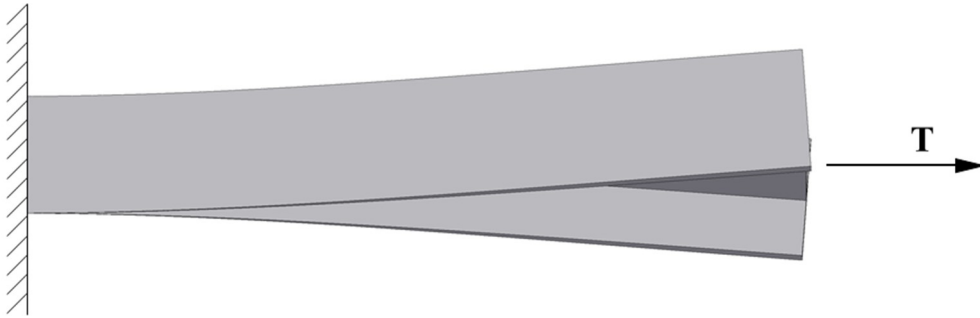


Figure 20. Restricted warping on an I-beam (according to Timoshenko 1940, p. 283)

The counter rotation is now fully restrained at the fixed end, from where the counter rotation gradually increases towards the free end. Therefore the flanges must bend in lateral direction and the torque is carried partly by the shearing stresses due to the twisting of the beam (pure torsion) and partly by the shearing stresses due to the bending of the flanges. The bending of the flanges adds to the overall rigidity of the beam compared to unrestricted torsion and therefore decreases the angle of twist. The significance of the bending effect of the flanges to the angle of twist depends on the rigidity of the flanges and the geometric proportions of the beam. The effect of the phenomena is the strongest at the root from where it gradually decreases as the free length increases. (Timoshenko 1940, p. 282 – 286.)

Figure 21 shows the restricted warping as seen from the free end of the beam. The picture also shows the relation between the angle of twist and the deflection of the flanges:

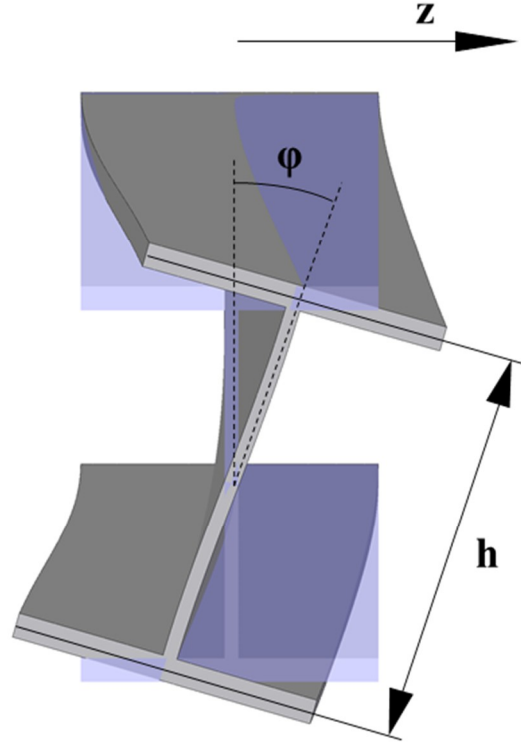


Figure 21. Restricted warping of an I-beam (according to Timoshenko 1940, p. 283)

In the picture the undeformed model is shown in light purple. From the geometry the lateral deflection of the upper flange can be given as (Timoshenko 1940, p. 284):

$$z \cong \frac{h}{2} \varphi \quad (41)$$

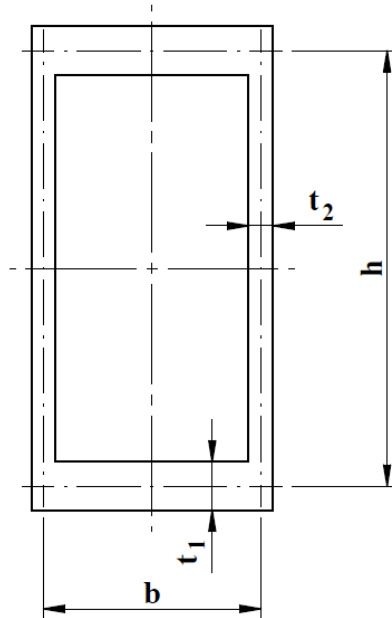
, where  $h$  is the distance between the centroids of the top and bottom flanges and  $\varphi$  the angle of twist. To obtain the shearing force due to bending of the flange requires differentiation of the equation to the third derivative to get the *rate of change of curvature*. The general equation for the torsional moment can be found as: (Hughes et.al. 2011, p. 14.)

$$\frac{T}{GI_v} = \varphi' - a^2 \varphi''' \quad (42)$$

, where  $\varphi'$  and  $\varphi'''$  are the first and third derivatives of the angle of twist and  $a$  is the torsional bending constant ( $a = \sqrt{EI_w/GI_v}$ ). It is a dimension of length and depends on the cross-

section geometry. It is an indicator of how quickly the effect of warping dissipates and when compared to the overall length of the beam, it gives a perception of the influence that warping restriction has to the total torsional deflection. Term  $I_w$  inside the square root is the warping constant; a value of dimension to the 6<sup>th</sup> power. It describes the cross-section geometry resistance to the torsion induced bending of the flanges. (Hughes et.al. 2011, p. 9 – 14.)

Formulas to determine  $I_w$  for different types of cross-sections can be found in Timoshenko & Gere (1963, p. 530), Valtanen 2019 (p. 364 – 365) or Rubin 2005 (p. 828 – 830). Hughes and Malik (2011, p. 13) list different cross-sections types according to their warping behaviour: With double flanged sections (I and H-beams) the warping effect is the most notable, but in closed rectangular hollow sections (with typical dimensions) the warping effect is usually negligible as it is also with angled sections such as L, T or X. For a square hollow section the primary warping function actually vanishes (returns zero) and therefore isn't considered (Bauchau and Craig (2009, p. 375). The warping constant of a double symmetric rectangular hollow section (which concerns the structural analysis of this thesis) can be formulated from Rubin (2005, p. 828) as shown in figure 22:



$$I_w = \frac{1}{24} b^2 h^2 \left( \frac{ht_1 - bt_2}{ht_1 + bt_2} \right)^2 (ht_1 + bt_2) \quad (43)$$

Figure 22. Warping constant of a double symmetric rectangular cross-section (formulated from Rubin 2005, p. 828)

From the equation can be seen that when  $ht_1$  and  $bt_2$  are equal, the warping function returns zero, which is the case in a square hollow section with uniform wall thickness.

By solving the differential equation 41 (page 34) for the variation of the angle of twist at the distance  $x$  along the beam, the solution has a form (Hughes et.al. 2011, p. 69):

$$\varphi(x) = A \sinh\left(\frac{x}{a}\right) + B \cosh\left(\frac{x}{a}\right) + C_1 x^3 + C_2 x^2 + C_3 x + C_4 \quad (44)$$

, where  $C_{1...4}$  are integration constants, which depend on the boundary conditions of the beam. In the structural analysis of this thesis it is assumed that the section is rigidly supported at one end and free at the other. By applying these boundary conditions, the formula for the angle of twist can be found as (Hughes et.al. 2011, p. 74):

$$\varphi(x) = \left(\frac{Ta}{GI_v}\right) \left\{ \tanh\left(\frac{L}{a}\right) \left[ \cosh\left(\frac{x}{a}\right) - 1 \right] - \sinh\left(\frac{x}{a}\right) + \frac{x}{a} \right\} \quad (45)$$

, where  $T$  is the applied moment and  $x$  the distance from the fixed end.

## 2.4 Distortion of a cross-section

As a fourth strain type to consider in addition to bending, shear and torsion would be distortion of the cross-section. It is a phenomena caused by asymmetric load distribution and according to Kermani & Waldron (1993, p. 427 – 428) it is a characteristic behaviour for thin-walled sections and may be triggered even by a single point load, if it's placed eccentrically in respect to the centroid plane. Distortion is additional to torsional warping and occurs where the cross-section is permitted to deform. In Figure 23 is shown an example how the distortion effect appears in a square box beam under eccentric point load:

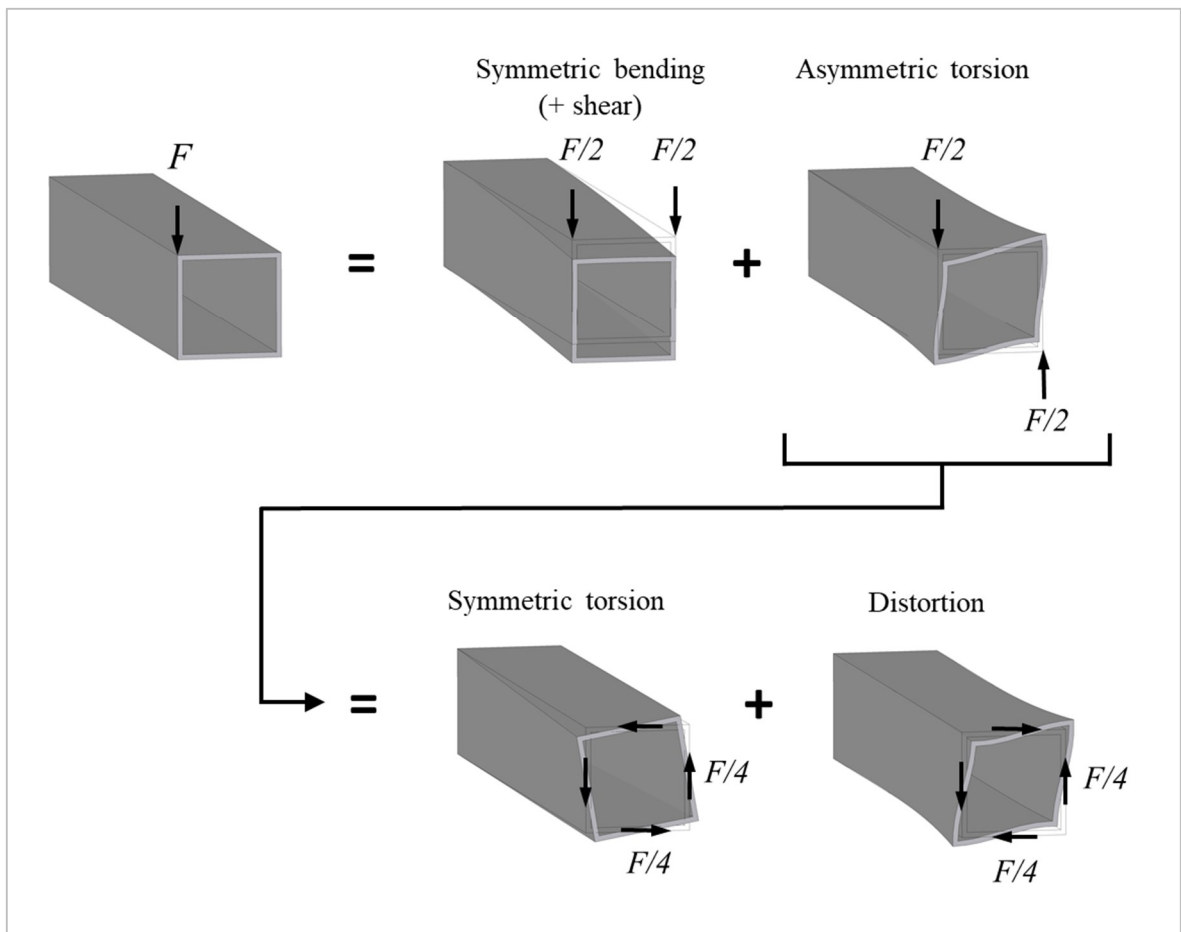


Figure 23. Distortion of a cross-section (according to Zhu et.al. 2020, p. 2)

On the left in the picture is shown a SHS cantilever beam loaded with an eccentric point load  $F$ . This load is first divided into symmetric transverse load and asymmetric torsion load. Then the asymmetric torsion load is further divided into symmetric torsion load and distortion (Zhu et.al. 2020, p. 2). The magnitudes of the force vectors are adjusted in each step so that the final sum equals with the initial point load  $F$ . In the example the distorting forces cause the cross-section to distort from a square shape into a parallelogram and the walls of the section to deform into S-shape as the picture shows. To restrict the distortion of the cross-section, a diaphragm plate may be used, which locks the two diagonals together and prevents the S-deformation of the walls of the section. Remarking the possible distortional behaviour of the cross-section is important not only from the displacement point of view, but also that it creates stress concentration at the corners of the cross-section, which should be considered especially if the load is fluctuating nature and the section is built as a welded assembly. (Björk et.al. 2020, p. 5 – 10.)

## 2.5 Estimating sheet transition at the punching center

One way to estimate the sheet movement at the punching center during frame deflection is to use a coordinate system transformation. By choosing a global reference frame to the punching center and a local reference frame to the end of the frame, the movement of the sheet during the frame deflection can be tracked in respect to the punching center. The rough locations of the coordinate systems are shown in Figure 24 below:

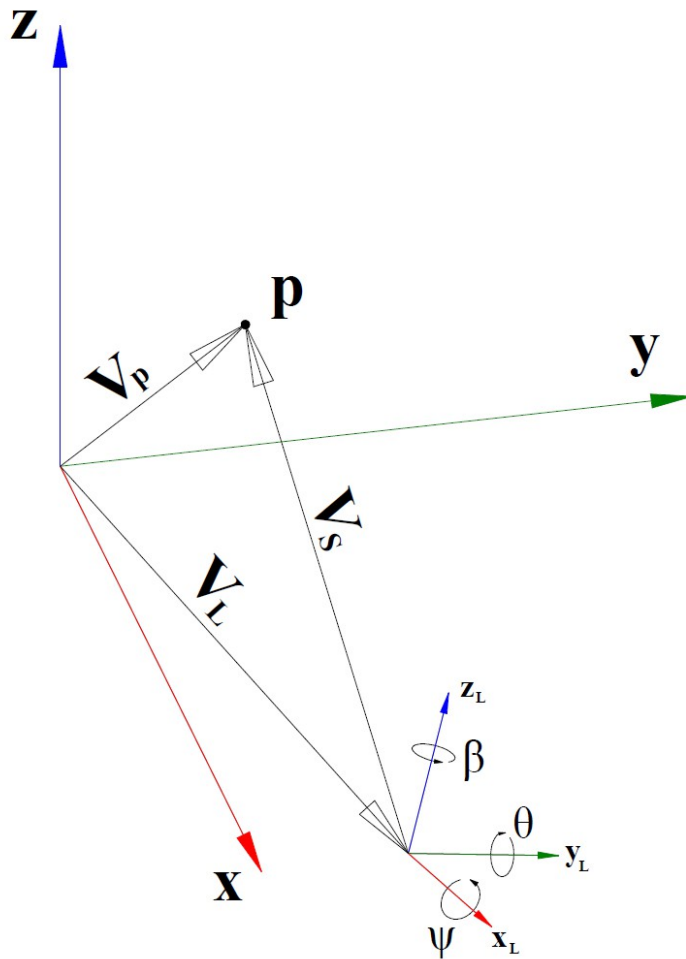


Figure 24. Transformation from local to global coordinate system

In the picture the local coordinate system ( $x_L$ ,  $y_L$ ,  $z_L$ ) is attached to the axis of twist of the frame structure and vector *V<sub>s</sub>* marks the reference point *p* at the corner of the sheet, which before deflection was located at the global origin. Vector *V<sub>L</sub>* positions the origin of the local coordinate system during deflection. Angle  $\psi$  is the angle of twist due to torsion, and  $\beta$  the slope of the deflection curve. The rotation of a coordinate system is done by projecting the

vector  $\mathbf{V}_s$  components to the global system using *sin* and *cosine* functions repeatedly for each axis rotation. Commonly used order for the rotations is the roll-pitch-yaw (or Z-Y-X) sequence, where the orientation of the coordinate system is determined by rotating each axle once. Below are shown the rotation matrices for each sequence (Siciliano et.al. 2009, p. 42):

$$\begin{aligned} [\mathbf{R}_z] &= \begin{bmatrix} \cos(\beta) & -\sin(\beta) & 0 \\ \sin(\beta) & \cos(\beta) & 0 \\ 0 & 0 & 1 \end{bmatrix} \\ [\mathbf{R}_y] &= \begin{bmatrix} \cos(\theta) & 0 & \sin(\theta) \\ 0 & 1 & 0 \\ -\sin(\theta) & 0 & \cos(\theta) \end{bmatrix} \\ [\mathbf{R}_x] &= \begin{bmatrix} 1 & 0 & 0 \\ 0 & \cos(\psi) & -\sin(\psi) \\ 0 & \sin(\psi) & \cos(\psi) \end{bmatrix} \end{aligned}$$

The complete rotation matrix  $[\mathbf{R}]$  is a multiplication of the three ( $R = R_z R_y R_x$ ). The angle  $\theta$  around the y-axis would be zero in this particular coordinate transformation case and therefore with  $\theta = 0$  the matrix  $[\mathbf{R}_y]$  would be reduced to identity making it unnecessary to include in the rotation matrix, but below is shown the rotation matrix in its complete form (all three rotations included):

$$\begin{aligned} [\mathbf{R}] &= [\mathbf{R}_z] \times [\mathbf{R}_y] \times [\mathbf{R}_x] \\ &= \begin{bmatrix} \cos(\beta) \cos(\theta) & \cos(\beta) \sin(\theta) \sin(\psi) - \sin(\beta) \cos(\psi) & \cos(\beta) \sin(\theta) \cos(\psi) + \sin(\beta) \sin(\psi) \\ \sin(\beta) \cos(\theta) & \sin(\beta) \sin(\theta) \sin(\psi) + \cos(\beta) \cos(\psi) & \sin(\beta) \sin(\theta) \cos(\psi) - \cos(\beta) \sin(\psi) \\ -\sin(\theta) & \cos(\theta) \sin(\psi) & \cos(\theta) \cos(\psi) \end{bmatrix} \end{aligned}$$

From here the coordinates for the point  $p$  in the global coordinate system can be given as:

$$[\mathbf{V}_p] = \begin{bmatrix} x \\ y \\ z \end{bmatrix} = [\mathbf{V}_L] + [\mathbf{R}] \times [\mathbf{V}_S] \quad (46)$$

For example, if the initial local origin of the frame structure where the sheet is attached is found at [2150, 1270, -480] (mm) measured from the punching center and then the frame would first deflect 0.05 mm in y-direction, the vector  $\mathbf{V}_L$  would be [2150; 1270.05; -480]<sup>T</sup> (mm). In addition to transverse deflection the frame would also be

bent according to the deflection slope so that rotation around z-axis is -0.0001 and finally the torsion rotation around x-axis would be +0.0002 radians; The corresponding angles  $[\beta, \theta, \psi]$  for rotation matrix are then  $[-0.0001; 0; 0.0002]$ . The vector  $\mathbf{V}_S$  marking the reference point in the sheet at the punching center in a local coordinate system is the same as  $\mathbf{V}_L$  but only to opposite direction:  $[-2150; -1270; 480]^T(\text{mm})$ . Inserting the vectors and angles to the equation, the coordinates for point  $p$  are obtained as:  $[\mathbf{V}_p] \approx [-0.127; 0.169; -0.254]^T(\text{mm})$  and the total positioning error in x-y-plane would be:  $\sqrt{\Delta x^2 + \Delta y^2} \approx 0.211 \text{ mm}$ .



### 3 Results from analytical calculations

In the following are presented results obtained from analytical calculations. The maximum transverse and torsion deflection are calculated for a group of cross-sections according to the load caused by the system acceleration. The obtained results are then inserted into a coordinate system transformation which shows the theoretical movement of the sheet at the punching center due to the frame deflection.

#### 3.1 Model description

Structural model used for the calculation is shown in Figure 25:

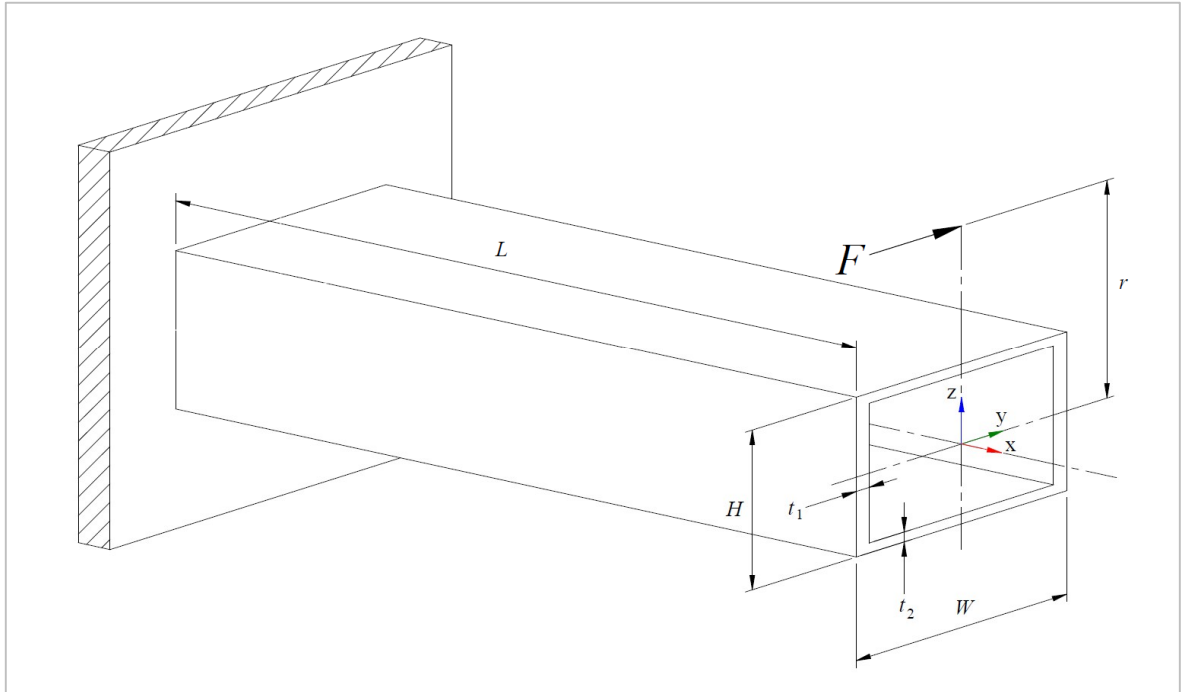


Figure 25. Structural model for calculation

In the picture the model is loaded by a lateral force  $F$ , placed at distance  $r$  from the centroid, which is also the center of twist in a double symmetric section.  $t_1$  and  $t_2$  are the wall thicknesses for the side plates and top/bottom plates.  $H$  and  $W$  mark the overall height and width taken from the free surfaces.  $L$  is the length of the section. The section is rigidly supported at the root. Calculation constants are listed in Table 1:

Table 1. Calculation constants

$F$ (N)	$L$ (mm)	$H$ (mm)	$r$ (mm)	$E$ (MPa)	$G$ (MPa)
10000	2150	350	520	210000	80000

Section width ( $W$ ) and wall thicknesses  $t_1$  and  $t_2$  are chosen as variables. Width is set to vary from 400 mm to 1000 mm by 100 mm increments. Wall thicknesses range from 20 mm to 30 mm by 5 mm increments uniformly for both  $t_1$  and  $t_2$ ; this makes a total of 21 different cross-sections for analytical calculations.

### 3.2 Transverse deflection and slope of the deflection curve

The second moment of area  $I$  needed for the calculation is deduced simply by subtracting the hollow zone of the cross-section from the value calculated by the outer dimensions:

$$I_{z-z} = \frac{HW^3 - hw^3}{12} \quad (47)$$

, where  $h = H - 2t_2$  and  $w = W - 2t_1$ . Bending deflection and slope of the flexure curve are calculated by eq. 12 & 13 (page 16). For shear deflection, the formulas based on the first moment of area are used (eq. 23, 25 & 27, pages 23 – 24). Results are shown in the next page in a chart format (Figure 26):

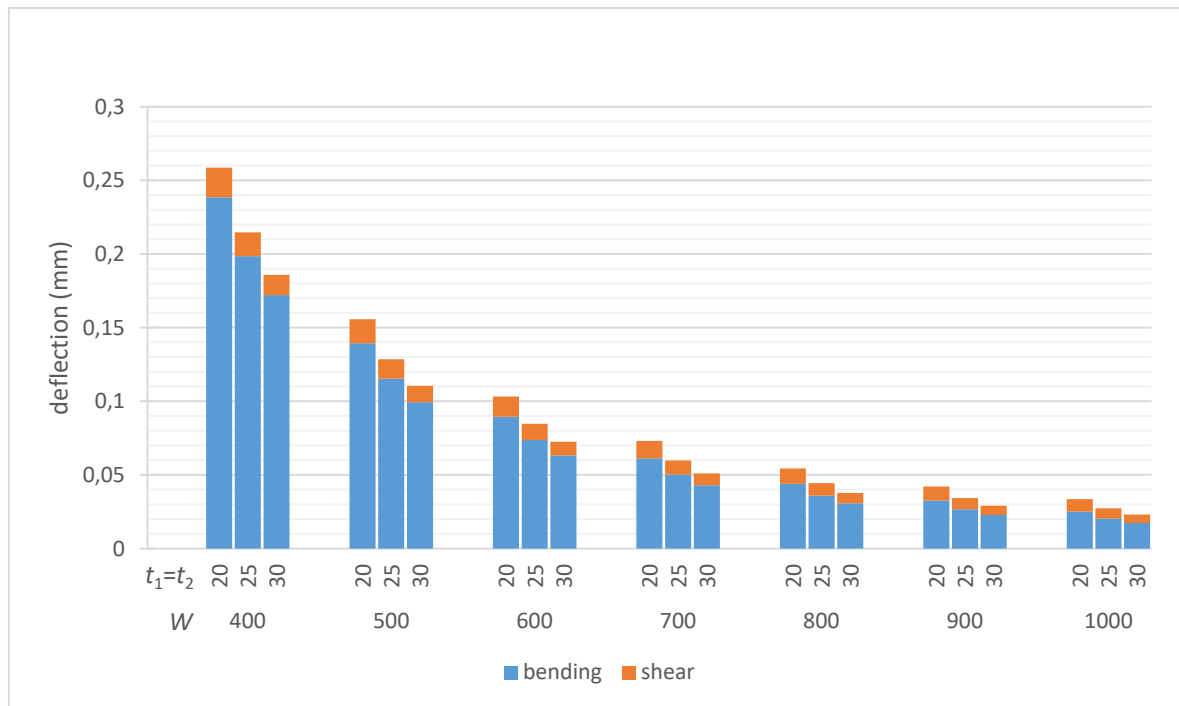


Figure 26. Transverse deflection

The figure shows the magnitude of the bending and shear deflection as stacked columns. In the chart the cross-sections are divided into groups according to their width (400 mm → 1000 mm) and within each group there are three columns which mark the deflection with each wall thickness. Results show that as the width of the cross-section increases, the deflection decreases significantly. The flexure in the narrowest cross-section is about 8 times greater than in the widest one. The “slope” of the graph decreases towards the end as the proportional change in width from the previous section to the next one decreases. On the next page are shown the same results in a table format (Table 2):

Table 2. Transverse deflection and slope of the deflection curve

$W$ (mm)	$t_1=t_2$	bending (mm)	shear (mm)	total (mm)	slope (rad)
400	20	0.2385	0.0201	0.2586	0.0001758
	25	0.1985	0.0163	0.2148	0.0001460
	30	0.1721	0.0137	0.1858	0.0001264
500	20	0.1394	0.0163	0.1557	0.0001048
	25	0.1153	0.0131	0.1285	0.0000866
	30	0.0994	0.0111	0.1104	0.0000745
600	20	0.0895	0.0137	0.1032	0.0000688
	25	0.0737	0.0111	0.0848	0.0000566
	30	0.0632	0.0093	0.0725	0.0000484
700	20	0.0612	0.0119	0.0731	0.0000482
	25	0.0503	0.0096	0.0598	0.0000395
	30	0.0430	0.0080	0.0510	0.0000337
800	20	0.0439	0.0105	0.0544	0.0000355
	25	0.0360	0.0085	0.0444	0.0000290
	30	0.0307	0.0071	0.0378	0.0000247
900	20	0.0327	0.0094	0.0421	0.0000272
	25	0.0267	0.0076	0.0343	0.0000222
	30	0.0227	0.0064	0.0291	0.0000188
1000	20	0.0250	0.0086	0.0336	0.0000214
	25	0.0204	0.0069	0.0273	0.0000174
	30	0.0173	0.0058	0.0231	0.0000148

In the table are listed round values for bending and shear deflection, total transverse deflection and the slope of the deflection curve, measured at the end of the section. The portion of shear deformation of the total deflection ranges from 7.5% to 25.6%, the smallest value being found in the narrowest section with  $t = 30$  mm. From there the share or shear deflection increases by the width of the cross-section and reaches the maximum of 25.6% in the 1000 mm wide section with 20 mm wall thickness. The slope of the deflection curve contains the combined action of bending and shear deformation: It is used as the rotation angle around z-axis when assessing the sheet displacement at the punching center.

### 3.3 Deformation due to torsion

Torsion deformation was calculated using both Saint-Venant (pure torsion) and warping torsion. For Saint-Venant torsion the torsion modulus  $I_v$  is calculated using Bredt's formula (eq. 35 on page 29), which is then placed to equation 34 (page 27) in place of  $I_p$ . The

following graph (Figure 27) shows the results for Saint-Venant torsion caused by the moment  $Fr$ :

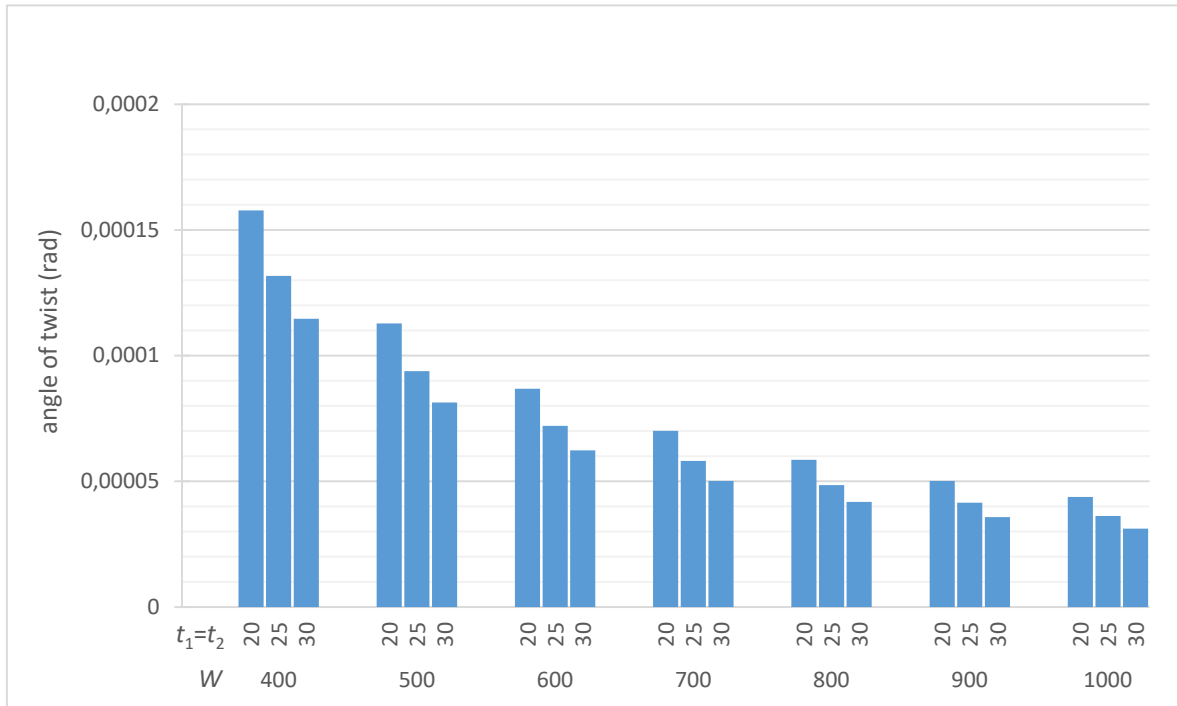


Figure 27. Deformation due to Saint-Venant torsion

The angle of twist ranges from 0.000158 to 0.000031 radians (calculated values) from the narrowest one ( $W = 400$ ,  $t = 20$  mm) to the widest one ( $W = 1000$ ,  $t = 30$ ). When sections with equal wall thicknesses are compared, the angle of twist in the widest section is around 73% smaller than in the narrowest one. As the assessment o8) is shown the resulting lateral displacement at 480 mm height from the axis of twist; this is the height where the punching center is located in reference to the frame.

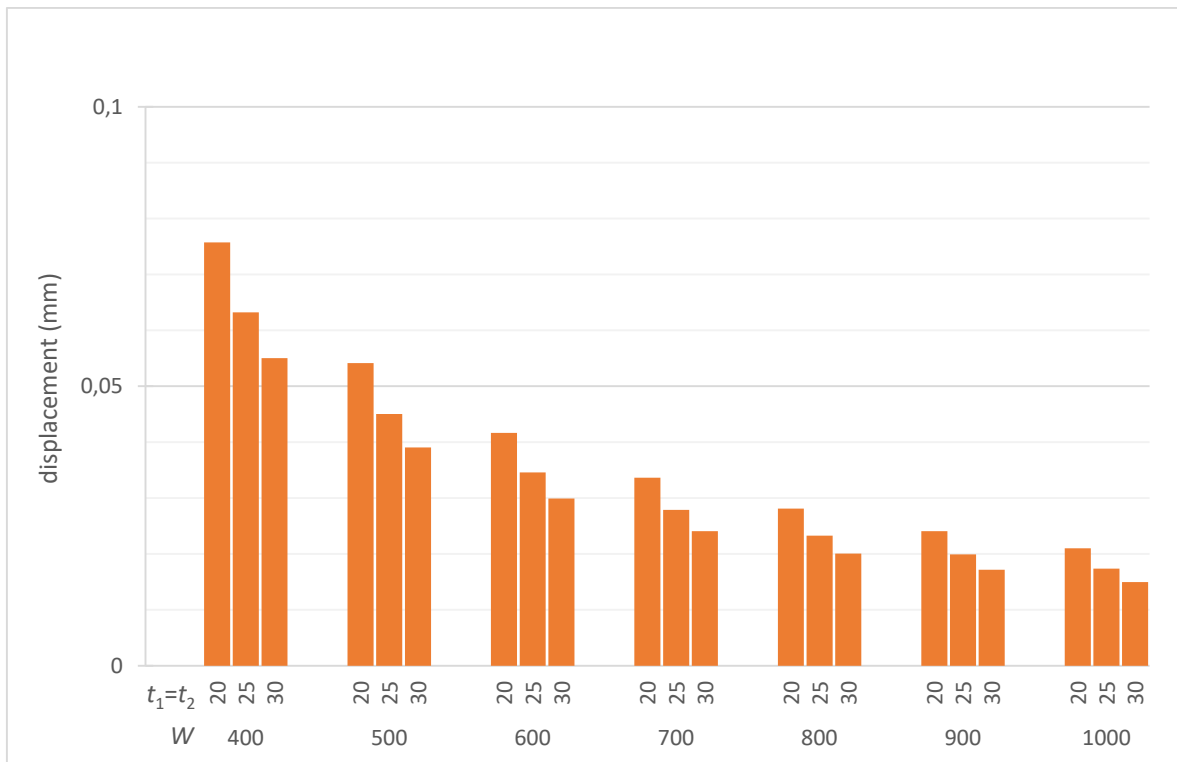


Figure 28. Saint-Venant torsion: Lateral displacement measured at 480 mm height from the axis of twist

The displacements are within same order of magnitude as the flexural displacement (bending + transverse shear), but with the narrowest section ( $W = 400$ ,  $t = 20$  mm) the flexural displacement is clearly dominating being about 3.4 times more than the torsional displacement. As the width of the section increases, the gap narrows down, yet in the widest section ( $W = 1000$  mm,  $t = 30$  mm) the displacement from bending and shear deformation is still 1.5 times higher than the displacement caused by torsion.

Corresponding graphs for warping torsion are not represented here as they follow very closely Saint-Venant solution, but they are included in Table 3 next, where is shown the percentage difference between Saint-Venant and warping torsion. Warping constant  $I_w$  and warping torsion are calculated here by equations 43 and 45.

Table 3. Saint-Venant torsion and warping torsion comparison

$W$ (mm)	$t_1=t_2$	Saint-Venant torsion (rad)	warping torsion (rad)	difference (%)
400	20	0.00015774	0.00015774	0.0 %
	25	0.00013172	0.00013172	0.0 %
	30	0.00011464	0.00011464	0.0 %
500	20	0.00011279	0.00011279	0.0 %
	25	0.00009382	0.00009382	0.0 %
	30	0.00008135	0.00008135	0.0 %
600	20	0.00008679	0.00008443	-2.7 %
	25	0.00007203	0.00007007	-2.7 %
	30	0.00006231	0.00006061	-2.7 %
700	20	0.00007008	0.00006741	-3.8 %
	25	0.00005808	0.00005587	-3.8 %
	30	0.00005016	0.00004825	-3.8 %
800	20	0.00005853	0.00005567	-4.9 %
	25	0.00004846	0.00004609	-4.9 %
	30	0.00004182	0.00003977	-4.9 %
900	20	0.00005013	0.00004713	-6.0 %
	25	0.00004147	0.00003899	-6.0 %
	30	0.00003576	0.00003362	-6.0 %
1000	20	0.00004376	0.00004067	-7.1 %
	25	0.00003619	0.00003363	-7.1 %
	30	0.00003119	0.00002898	-7.1 %

The last row shows, how much smaller the angle of twist from the warping torsion is compared to Saint-Venant torsion. The more the aspect ratio of the section diverges from a square, the more significant the effect of warping torsion becomes. With 400 and 500 mm wide sections the error is practically zero. The maximum difference between Saint-Venant and warping torsion is 7.1% in the widest section.

### 3.4 Sheet movement at the punching center

For the calculation of sheet movement at the punching center, the wall thickness was selected 25 mm to narrow down the number of candidates from 21 to 7. Based on the analytical results, the components for the vector  $\mathbf{V}_L$ , which marks the origin of the local reference frame placed at the centroid at the free end of the frame, are listed in Table 4:

Table 4. Components for the vector  $\mathbf{V}_L$ 

Section #	$x$ (mm)	$y$ (mm)	$z$ (mm)
1	2150	1270.2148	-480
2	2150	1270.1285	-480
3	2150	1270.0848	-480
4	2150	1270.0598	-480
5	2150	1270.0444	-480
6	2150	1270.0343	-480
7	2150	1270.0273	-480

Sections are numbered according to their width, where #1 section is 400 mm wide and #7 1000 mm wide. Components for the vector  $\mathbf{V}_S$  in a local reference frame are  $[-2150; -1270; 480]^T$ . Angles for the rotation matrix  $\mathbf{R}$  are listed in Table 5:

Table 5. Angles for the rotation matrix  $\mathbf{R}$ 

Section #	$\Psi$ (rad)	$\theta$ (rad)	$\beta$ (rad)
1	-131.72E-6	0	146.04E-6
2	-93.82E-6	0	86.58E-6
3	-72.03E-6	0	56.56E-6
4	-58.08E-6	0	39.52E-6
5	-48.46E-6	0	29.03E-6
6	-41.47E-6	0	22.15E-6
7	-36.19E-6	0	17.44E-6

The rows in the table are in the same order as were the vector  $\mathbf{V}_L$  components: rotations around x-, y-, and z-axis. Being a more conservative choice, values for the x-axis rotation are based on Saint-Venant torsion. By inserting the values into the rotation matrix, the x- and y-coordinates for the point  $P$  and the corresponding total displacement at the punching center are obtained as in Table 6:



Table 6. Displacement of the sheet at the punching center in x-y –plane

Section #	x (mm)	y (mm)	$\sqrt{x^2 + y^2}$ (mm)
1	0.185491	-0.035991	0.188950
2	0.109963	-0.012624	0.110686
3	0.071834	-0.002267	0.071869
4	0.050195	0.002749	0.050270
5	0.036864	0.005282	0.037241
6	0.028136	0.006562	0.028891
7	0.022145	0.007170	0.023276

Figure 29 below shows the same results placed in x-y –coordinate system grid:

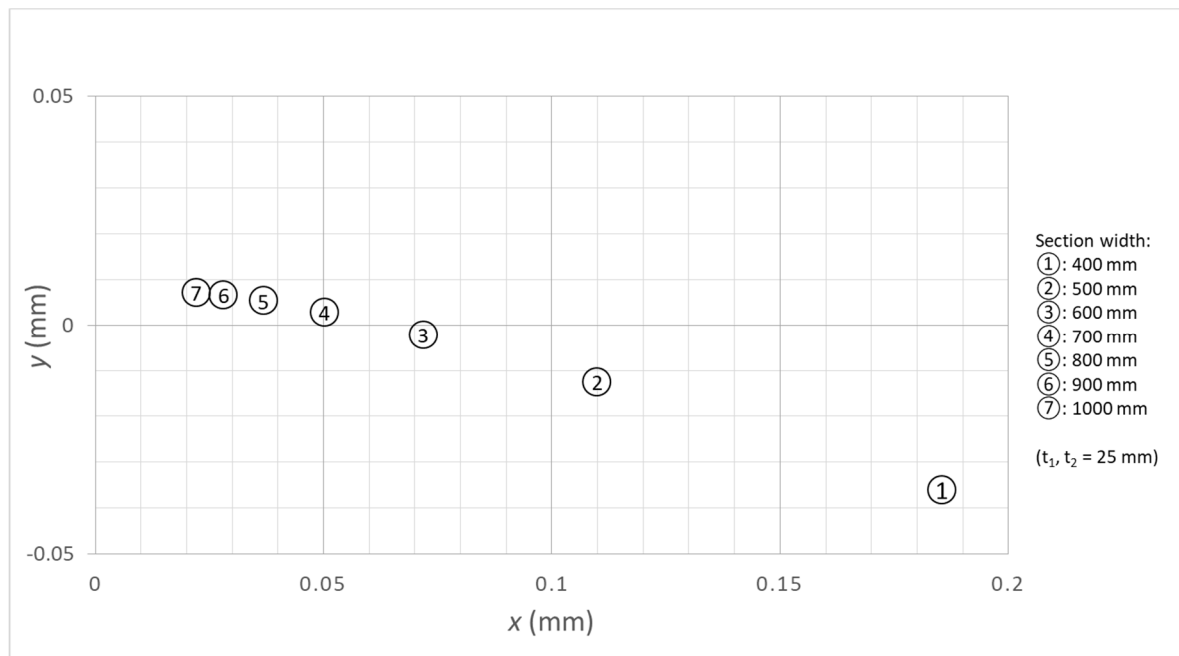


Figure 29. Displacement at the punching center

Total displacement varies from 0.023 mm (section #7) to 0.189 mm (section #1). The major share of the displacement comes from the change in x-coordinate and this value also ranges more significantly between sections than the y-coordinate, which with all sections stays within 0.04 mm. From the results can be noticed the effect of the rotation of the vector  $V_s$  according to the slope of the flexure curve: As the vector is being rotated, it compensates for the y-displacement, but at the same time the x-coordinate moves away from the initial zero position. With sections 1 – 3 the rotation actually overshoots the y-coordinate to the negative side, opposite to the force direction.

## 4 Results from FEM analysis

On the following are presented the results from the FEM analysis. Cross-section dimensions of section #6 are chosen as a basis for the FEM simulation. To get comparative results, the model is first tested with a single load type at a time. Then the model is further defined to represent more closely the actual application. In FEM, the model is also tested for structural modifications that either increase the stiffness by adding material, or decrease stiffness by removing material from places that could be required in the final construction. Apart from one exception, a surface mesh is used for FEM simulations, since it enables gathering results for both translational displacement and rotational displacement. For load attachment, an end plate with equal wall thickness as the rest of the model is used at the free end of the frame to avoid heavy distortion due to the force distribution. Simulations are done in Solid Edge® 2019 simulation environment. Meshing is done otherwise fully automatically except in some occasion the element quantity on an edge is assigned to an even number to position a node to the middle of the edge. On a scale 1 to 10 a value of 9 is used as the subjective mesh size. For Poisson's ratio a value 0.3 is used.

### 4.1 Deflection due to transverse force

Result due to transverse force is shown in Figure 30:

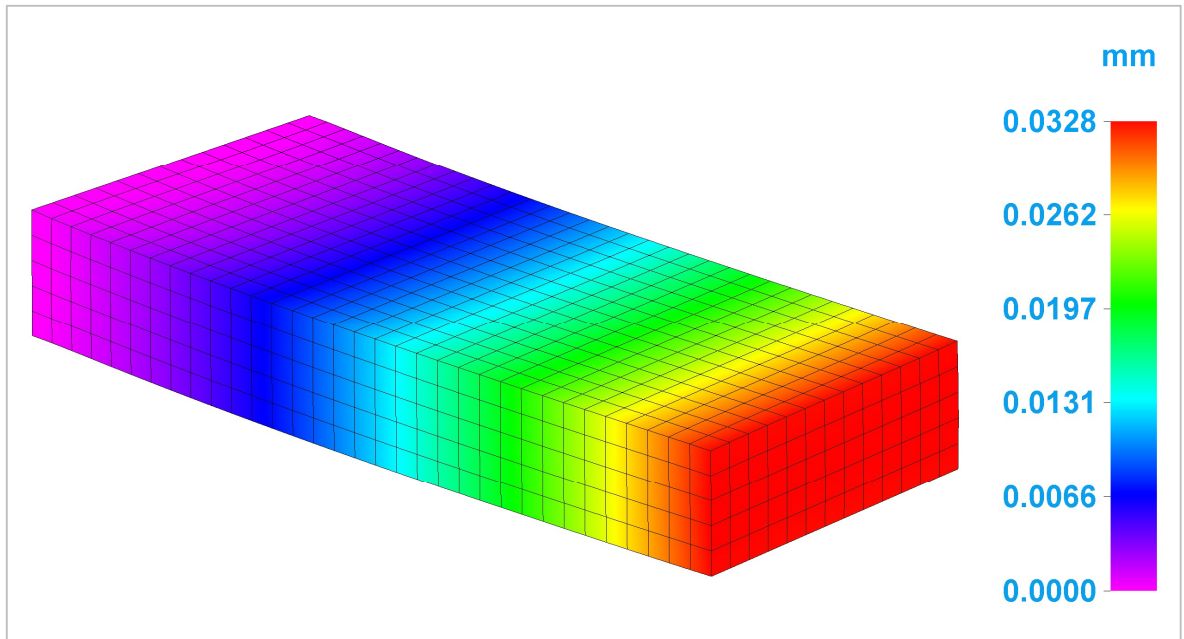


Figure 30. Transverse load: Y-displacement (Solid Edge® 2019)

The surface mesh model shown in the picture is made to the mid-planes of the solid model, so that the nodes at the free end are located at 2137.5 mm distance from the root ( $2150 \text{ mm} - 0.5t$ ). The load (10 000 N) is attached to the end face of the model. The maximum transverse deflection is 0.0328 mm, which is within 5% compared to the analytical result which was 0.0343 mm. The nodal rotation around z-axis due to the same transverse force is shown in Figure 31 below:

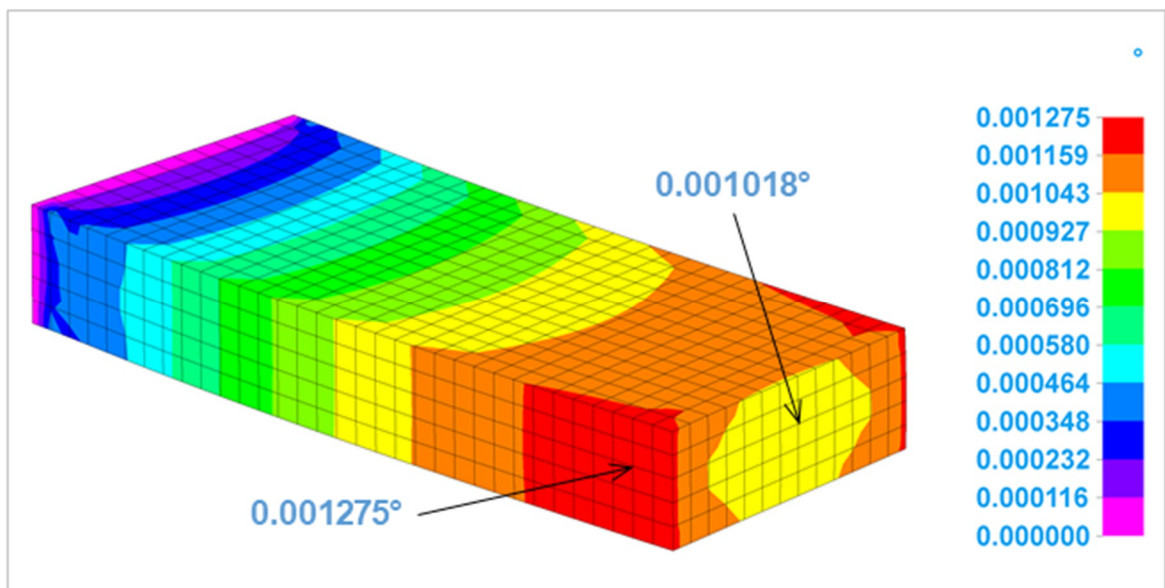


Figure 31. Transverse load: Nodal rotation around z-axis (Solid Edge® 2019, modified)

The mesh gives a maximum value of 0.001275 degrees located two elements away from the corner, which is within 1% when compared to the slope of deflection curve from analytical calculations. At the node next to the centroid plane the angle of rotation is 0.001018 degrees as marked in the picture. The surface mesh consists of 1272 nodes.

#### 4.2 Deformation due to torsion

Deformation due to torsion is shown in Figure 32:

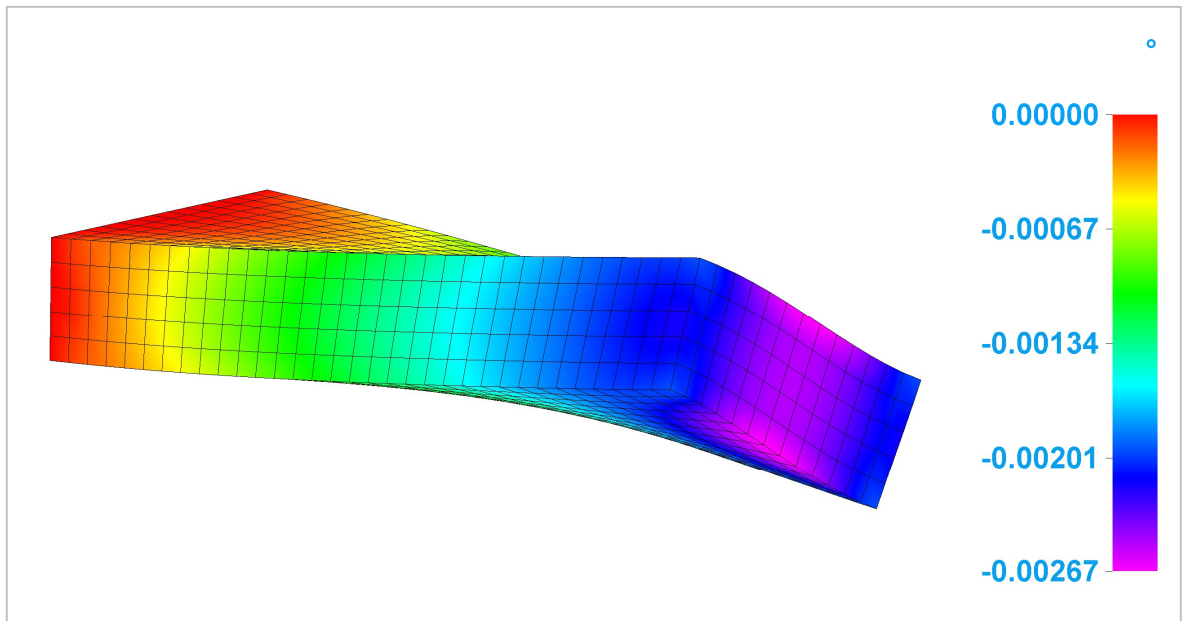


Figure 32. Torsion load: Nodal rotation around x-axis (Solid Edge® 2019)

In the picture the torque is applied to the face of the free end and the torque axis is set to the centroid line. The rotation degree varies at the end surface from around 0.00201 degrees to 0.00267 degrees. Angle of twist can be approximated also from the translational displacement at the side of the section ( $\Delta z$ ) by calculating the angle as  $\Psi = \Delta z / r$  where  $\Delta z$  is the deflection at distance  $r$  from the axis of twist. Vertical displacement was measured 0.0183 mm in the node closest the centroid plane so therefore:

$$\Psi = 0.0183 \text{ mm} / 437.5 \text{ mm} = 0.00004183 \text{ rad} \approx 0.00240 \text{ deg.}$$

The result is 2% more when compared to Saint-Venant solution (0.00238 degrees) and 8% more than the result from warping torsion which was 0.00223 degrees.

If the torque is applied without an end plate, the result is quite different. Figure 33 shows the vertical displacement of the same section under torsional loading, but the torque now applied to the cross-section without an end plate:

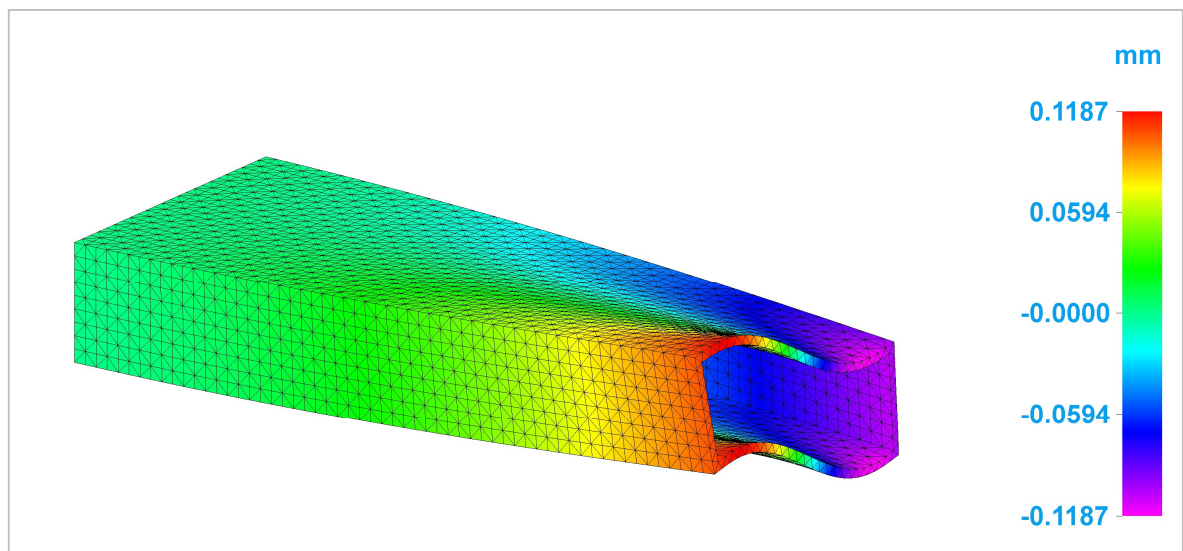


Figure 33. Torsion load: Deformation in z-axis direction without an end plate (Solid Edge<sup>®</sup> 2019)

In the picture can be seen the distorting effect of the torsion load as it is distributed to the end face. The resulting vertical deformation is almost 6.5 times greater than in the model with an end plate. In this simulation a tetrahedral mesh of 44936 nodes was used to place the torque to the cross-section.

#### 4.3 Diagonal bracing against torsion

In the chapter concerning structure under torsion, one design guideline was to use diagonal bracing. In Figure 34 is shown result for the angle of twist with single and double diagonal bracing:

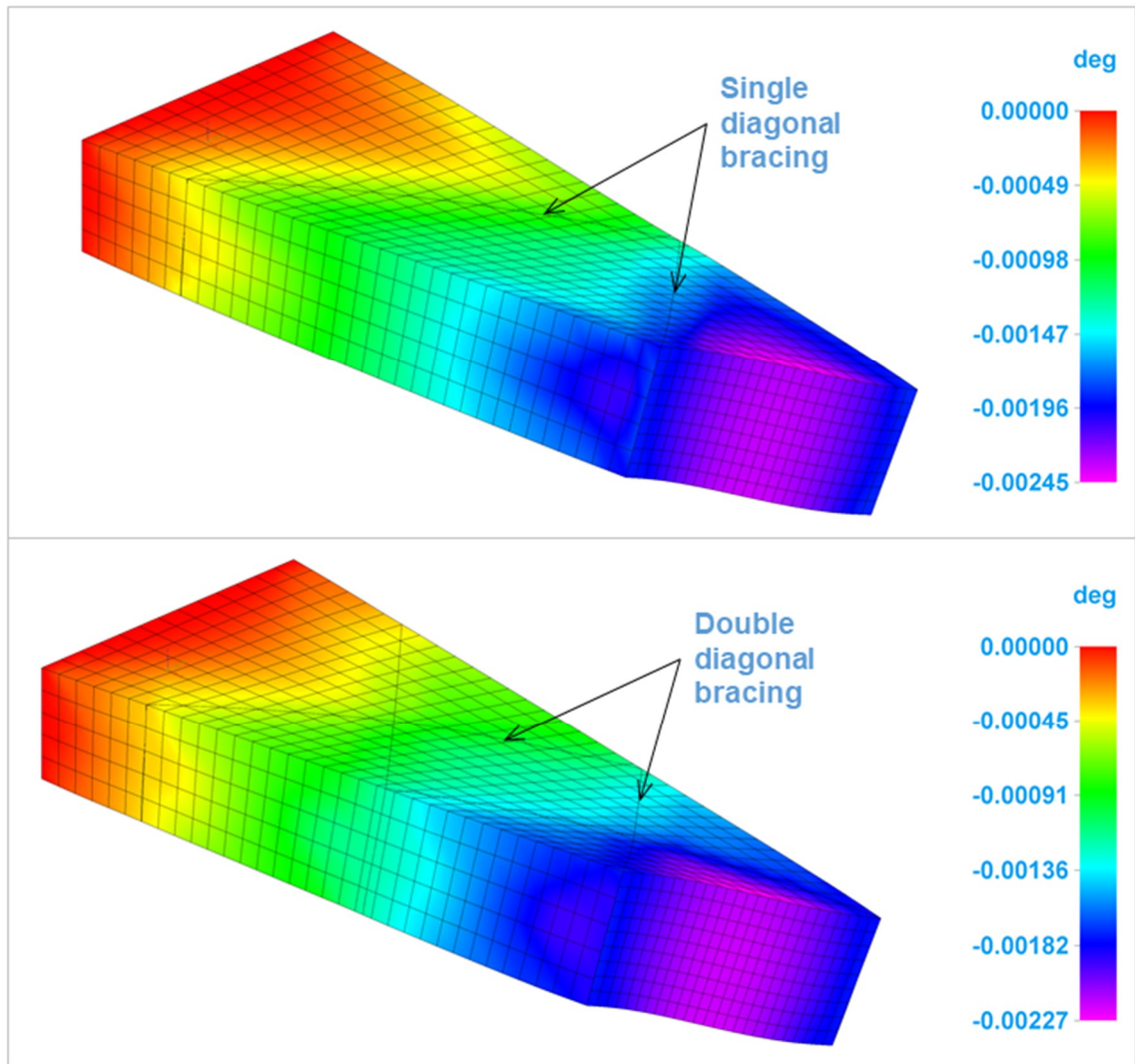


Figure 34. Torsion load: Nodal rotation around x-axis with diagonal bracing (Solid Edge® 2019, modified)

The wall thickness of the diagonal plates is the same as the cross-section: 25 mm. With single diagonal bracing (upper picture) the maximum angle of nodal rotation is 0.00245 degrees and with double diagonal bracing 0.00227 degrees. Values are 8% and 15% less compared to the surface mesh model without bracing, which had maximum value of 0.00267 degrees. The model with single diagonal bracing is made of 1932 nodes and the model with double diagonal bracing of 3876 nodes.

#### 4.4 Refining the FEM model

In the following the FEM model is further refined to represent more closely the actual application. The effect of diagonal and diaphragm bracing is also tested. Similarly the effect of cut outs at the sides of the frame is investigated. In the defined model the load vectors are placed using split-surfaces in the top of the model. The dimensions of the simulation model are shown in Figure 35 below:

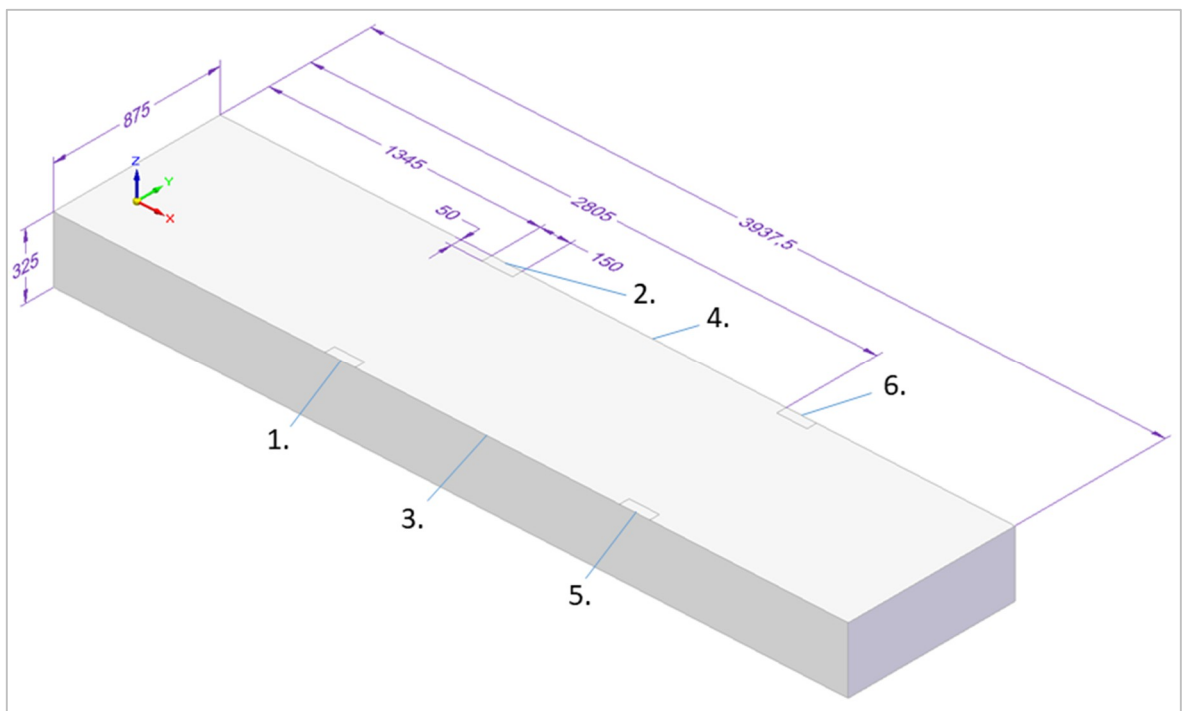


Figure 35. Dimensions of the simulation model (Solid Edge® 2019, modified)

The frame is still built as a mid-plane surface model, but the overall length is increased according to the application. To avoid force concentration only to few nodes, four independent rectangular segments of 150 x 50 mm are built to the top surface to represent the areas where the loads are assumed to go through. The segments are located symmetrically in respect to the 2150 mm x-coordinate, which was used as the beam length in the analytical calculations and which is the center of the moving mass. Numbers 1 – 6 refer to nodes from which the displacements are measured after each simulation. They are located at the outside edges of the mesh model. Nodes 1 – 2 and 5 – 6 are at the center of the load attachment surfaces and nodes 3 – 4 are the ones which are located closest to the center of the moving mass: With automated meshing the nodes were located roughly at 2130 mm from the origin.



When the sheet displacement at the punching center is later calculated, the rotation around x-axis and the y-displacement of the local reference frame  $V_L$  is defined by nodes 3 – 4. The rotation around z-axis is calculated according no nodes 1 – 5. As the sheet displacement is calculated according to the nodal coordinates, only translational displacement (y or z) are reported in the following simulations.

Figure 36 shows the simulation result for vertical displacement in a model without any additional bracing other than the end plate. The picture also shows the load placement:

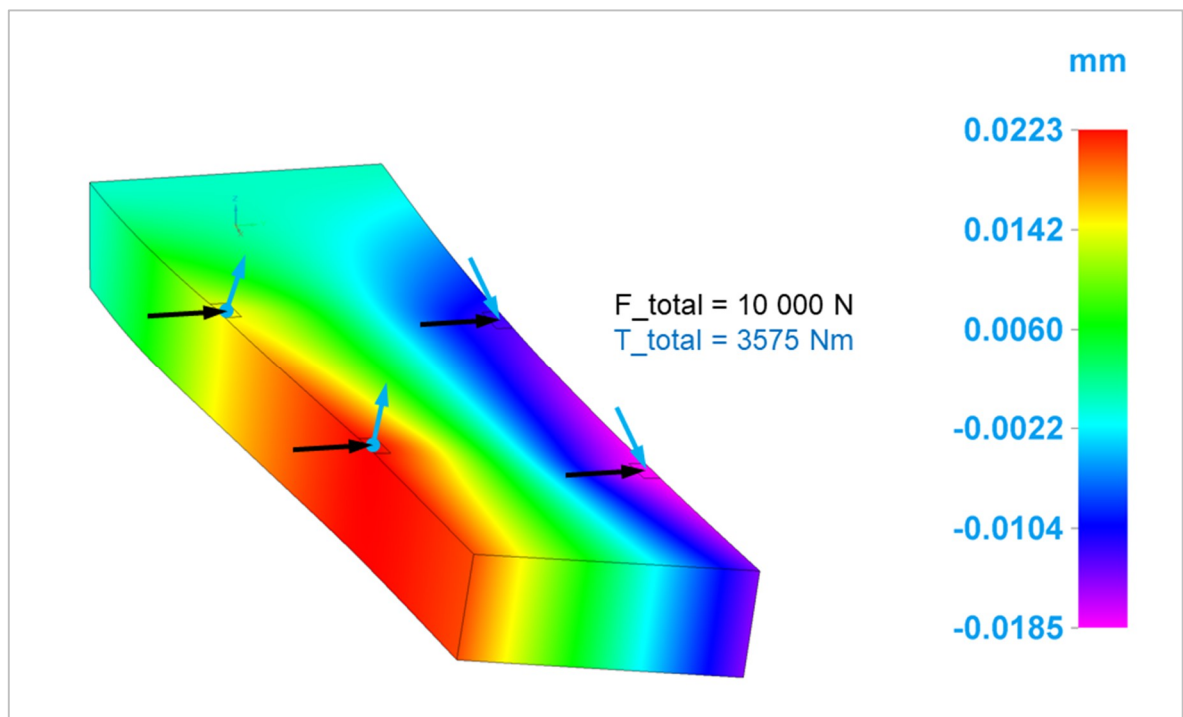


Figure 36. Vertical displacement without bracing and load attachment (Solid Edge® 2019, modified)

In the simulation all loads are defined as distributed loads within each segment – the single load vectors are drawn only for reference. As the transverse force isn't placed at the centroid plane anymore, it produces a moment which is subtracted from the additional torque requirement:  $5200\text{ Nm} - 0.1625\text{ m} \times 10000\text{ N} = 3575\text{ Nm}$ . The axis of torque is set to the centroid line of the cross-section. The mesh consists of 6219 nodes. Vertical displacement at the nodes mentioned in the previous page are listed in the following (in millimetres):



1. 0.0139
2. -0.0125
3. 0.0188
4. -0.0163
5. 0.0223
6. -0.0185

The results show that the displacement on the left side of the frame is more than on the right side. Difference varies from 11% to 15% to 21% according to the distance from the root, the smallest percentage difference representing nodes 1 and 2. To assess the angle of twist, a straight line is placed through nodes 3 – 4 and the angle of the line is calculated from:

$$\varphi \approx \text{atan}\left(\frac{z_2 - z_1}{y_2 - y_1}\right) \quad (44)$$

Taking the values from the listed results and using +/- 437.5 mm for the y coordinate, the angle of twist is found to be 0.00004011 radians or 0.00230 degrees. Results is 3% more than the analytical result from the warping torsion and 4% less than the result calculated from the surface mesh model shown in figure 33.

Results for horizontal displacement are shown in Figure 37:

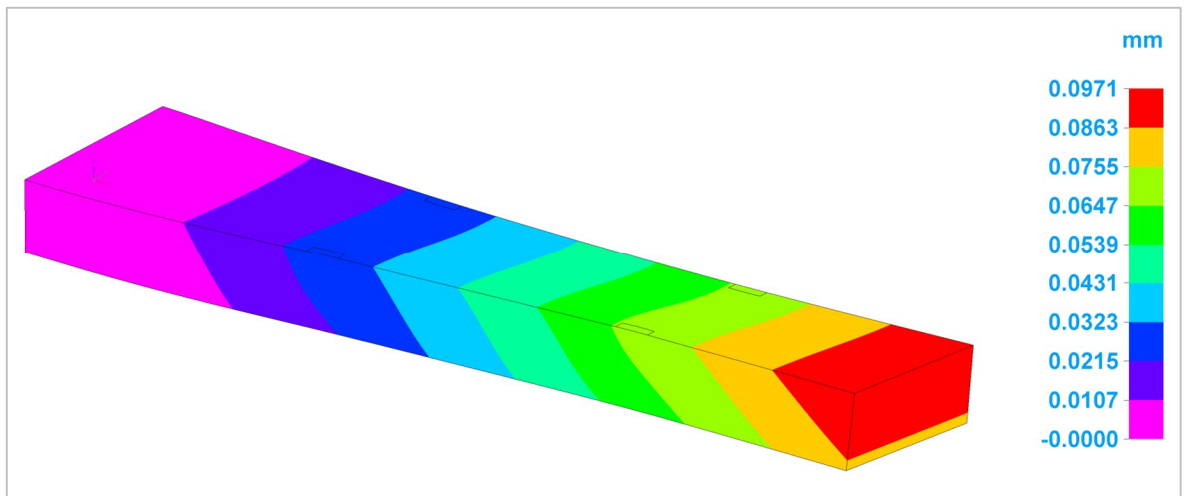


Figure 37. Y-displacement without bracing (Solid Edge® 2019)

A banded color bar is used to shown the inclined shape of the displacement variation across the height of the beam. Taking the exact values from the nodes 1 – 6, the horizontal displacements are (mm):

1. 0.0268
2. 0.0268
3. 0.0450
4. 0.0450
5. 0.0677
6. 0.0677

Although results are not directly comparable with previous simulations anymore, the displacement in points 3 – 4 is found 37% bigger than in the model in figure 31. The rotation around the z-axis, which is needed to assess the theoretical sheet movement at the punching center, is approximated similarly as the angle of twist in the previous by placing a line between two measured nodes: in this case the nodes 1 – 5. Taking the y-coordinates from the results above and the x-coordinates from the dimension sketch (figure 37) the angle of the line is given as:

$$\varphi \approx \text{atan}\left(\frac{0.0268 \text{ mm} - 0.0677 \text{ mm}}{1420 \text{ mm} - 2880 \text{ mm}}\right) \approx 0.00002801 \text{ rad}$$

The result is 26% greater than the one obtained from analytical calculations. By inserting the gathered results (rotation around x- and z-axis and the coordinates of vector  $\mathbf{V}_L$ ) to the coordinate system transformation matrices, the resulting sheet movement at the punching center is obtained as in Table 7:

Table 7. Displacement at the punching center (no additional bracing)

x (mm)	y (mm)	$\sqrt{x^2 + y^2}$ (mm)
0.035578	0.004027	0.035805

The result for the total displacement places between sections #6 (0.029 mm) and #5 (0.037 mm) from the analytical calculations.

#### 4.4.1 Diagonal bracing

Results for vertical and horizontal deflection using diagonal bracing (single type) are shown in Figure 38 below. Model contains four 25 mm thick diagonal plates which are placed at 45 degree angle, starting from the root. The mesh consists of 7115 nodes.

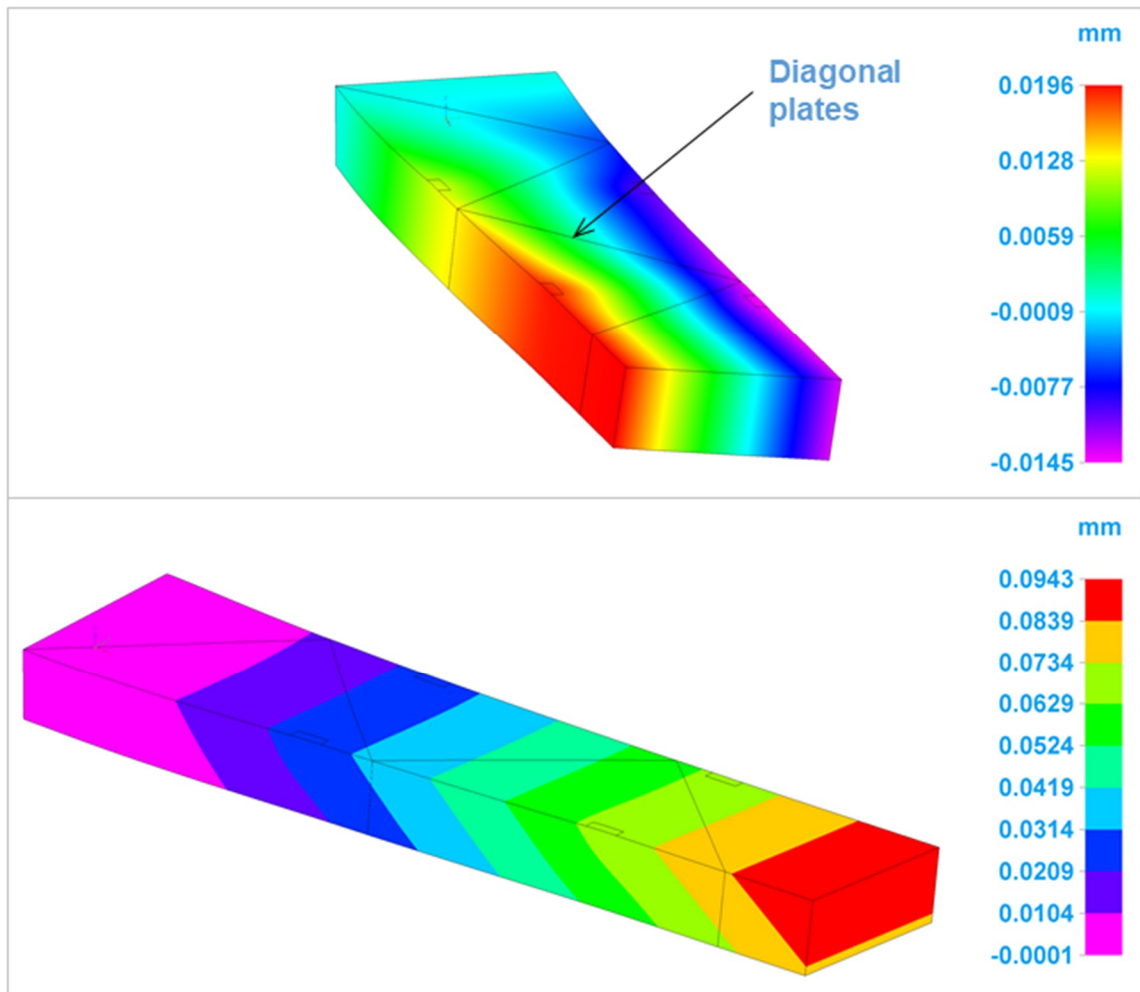


Figure 38. Z- and y-displacement with single diagonal bracing (Solid Edge® 2019, modified)

The exact results for the nodes are shown in Table 8, which contains also the percentage difference when compared to the model without bracing:

Table 8. Z- and y-displacement with single diagonal bracing and comparison to the model without bracing

Node	$\Delta z$ (mm)	% change	$\Delta y$ (mm)	% change
1	0.0115	-17.3 %	0.0263	-1.9 %
2	-0.0100	-20.0 %	0.0263	-1.9 %
3	0.0150	-20.2 %	0.0446	-0.9 %
4	-0.0125	-23.3 %	0.0446	-0.9 %
5	0.0189	-15.2 %	0.0666	-1.6 %
6	-0.0145	-21.6 %	0.0666	-1.6 %

The added torsional rigidity from the diagonal bracing improved the results for vertical displacement between 15 – 23%. The y-displacement, however, stayed within 2% compared to the model without bracing. The calculated sheet displacement at the punching center with diagonal bracing is shown in Table 9:

Table 9. Displacement at the punching center (diagonal bracing)

$x$ (mm)	$y$ (mm)	$\sqrt{x^2 + y^2}$ (mm)
0.035056	0.000341	0.035058

The improved in the total displacement compared to the model without bracing is under one thousand of a millimetre, so it has no practical effect on the accuracy.

#### 4.4.2 Diaphragm bracing

In the next the model is tested with diaphragm bracing. Here two 25 mm thick plates are positioned in the middle of the load attachment surfaces perpendicularly by the centroid line. The simulation result is shown in Figure 39. The mesh consists of 6739 nodes.

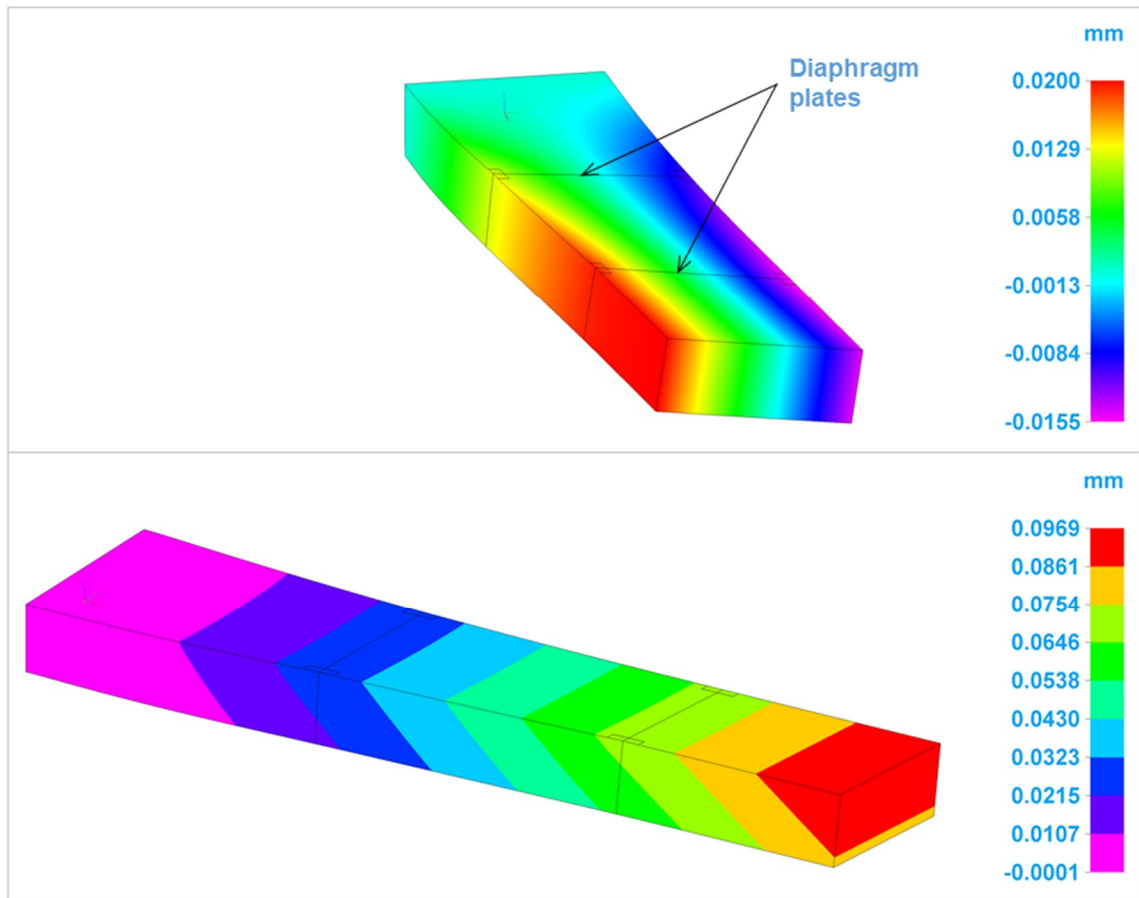


Figure 39. Z- and y-displacement with diaphragm bracing (Solid Edge® 2019, modified)

The maximum vertical displacement shown in the color bar is 2% more, and horizontal displacement 3% more than in the previous model with diagonal bracing. Measured values at the nodes are listed in Table 10 below:

Table 10. Z- and y-displacement with diaphragm bracing and comparison to model without bracing

Node	$\Delta z$ (mm)	% change	$\Delta y$ (mm)	% change
1	0.0119	-14.4 %	0.0274	2.2 %
2	-0.0105	-16.0 %	0.0274	2.2 %
3	0.0158	-16.0 %	0.0461	2.4 %
4	-0.0134	-17.8 %	0.0461	2.4 %
5	0.0192	-13.9 %	0.0687	1.5 %
6	-0.0155	-16.2 %	0.0687	1.5 %

Similarly to diagonal bracing the biggest improvement is in vertical displacement, where the improvement varies between 14 – 18%. However, on horizontal displacement the values are

actually higher than without bracing, but the difference is within 2.4%. Similar increase in displacement wasn't seen at the end of the frame though, so the increase in displacement seems to be local. The calculated sheet displacement at the punching center is shown in Table 11 below:

Table 11. Displacement at punching center (diaphragm bracing)

$x$ (mm)	$y$ (mm)	$\sqrt{x^2 + y^2}$ (mm)
0.035923	0.001301	0.035950

Again, there is no meaningful difference in the total displacement compared to the original model. The most notable effect of the diaphragm bracing can be seen when comparing the nodal rotation around x-axis side by side with the model without bracing (Figure 40):

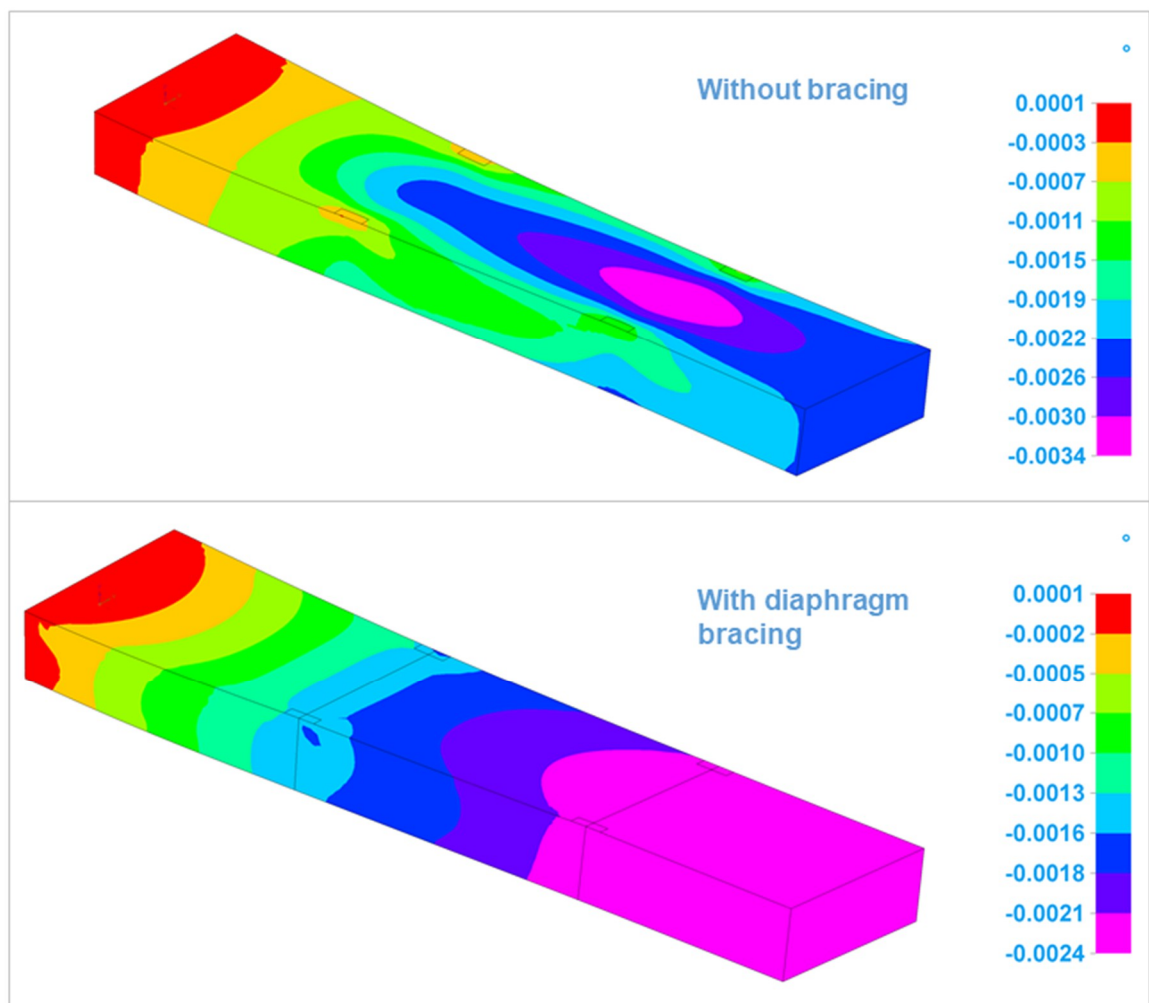


Figure 40. Nodal rotation around x-axis (Solid Edge® 2019, modified)

The model without bracing is shown in the upper picture, where there is a clearly defined blue – magenta zone in the middle of the top plate. Similar effect was also seen in the bottom plate, although in a more moderate fashion. Result indicates that the top and bottom plates distort into S-shape as in figure 32, page 53. With diaphragm bracing (bottom picture) the distortion is restrained at the diaphragm plates. One way to evaluate the magnitude of distortion is to calculate the difference of diagonals in a cross-section. Taken from nodes 3 and 4 to the opposite corners of the section, the difference in the diagonals is calculated to be 0.00972 mm in the model without bracing. With diaphragm bracing the difference is 0.00129 mm, which is 87% less than without bracing. The diagonals were also measured with the transverse force applied only: There the difference in diagonals was measured 0.01834 mm in the model without bracing, which is almost 2 times more than in the final simulation, where the additional torque is also present. The phenomena is further discussed in chapter 5.

#### 4.4.3 Effect of cut outs

In the final structure there might be a need for access to the inside of the frame to carry out installation of some accessory equipment. For this purpose two pieces of 200x100 mm cut outs are placed through the sides of the frame making four cut outs total. Cut outs are placed so that the first one is midway from the root to the first load attachment surface, and the second one midway between the two load attachment surfaces. Figure 41 shows the result when the cut outs are applied to the frame without any additional bracing. The mesh consists of 11420 nodes.

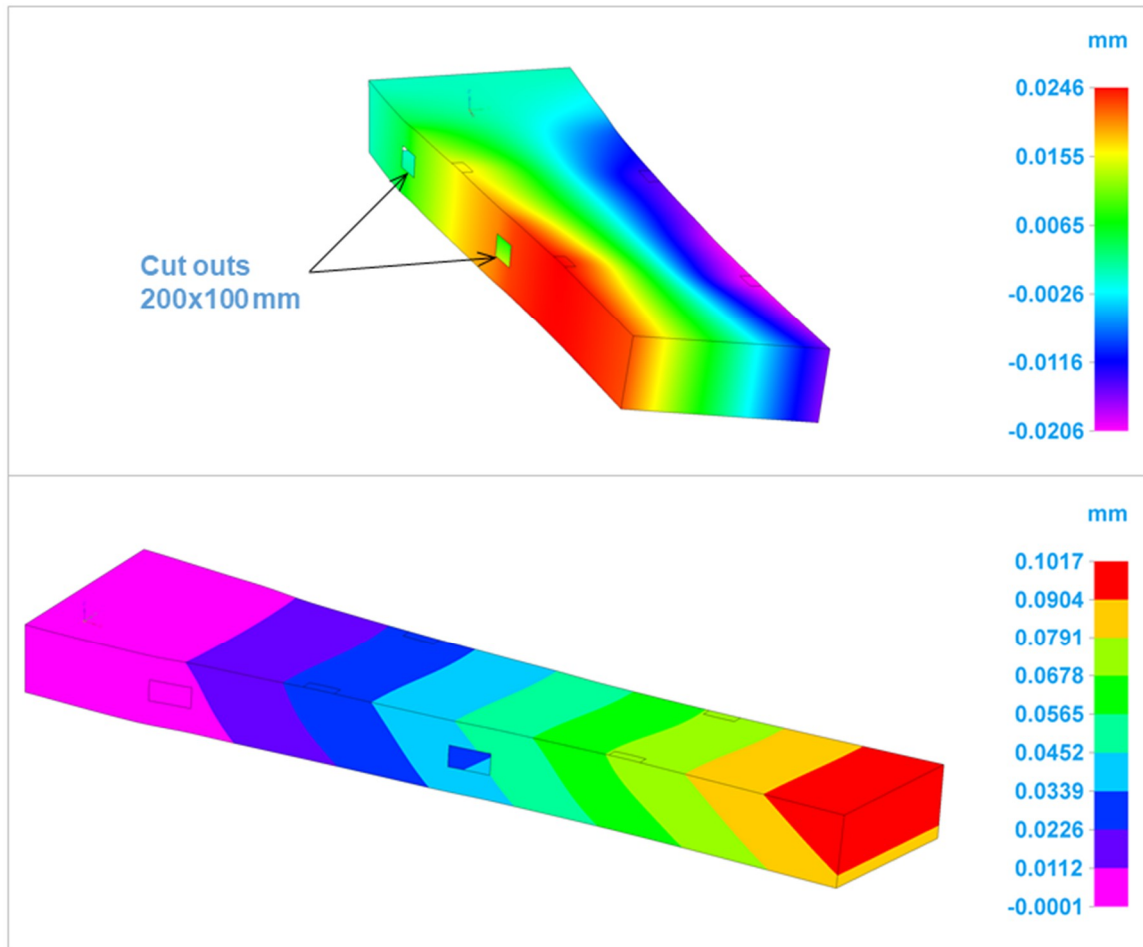


Figure 41. Z- and y-displacement with cut outs and no bracing (Solid Edge® 2019, modified)

In Table 12 below is shown the results for the displacement of the nodes:

Table 12. Z- and y-displacement with cut outs and no bracing compared to the original model (no cut outs, no bracing)

Node	$\Delta z$ (mm)	% change	$\Delta y$ (mm)	% change
1	0.0157	12.9 %	0.0278	3.7 %
2	-0.0143	14.4 %	0.0278	3.7 %
3	0.0206	9.6 %	0.0471	4.7 %
4	-0.0181	11.0 %	0.0471	4.7 %
5	0.0245	9.9 %	0.0707	4.4 %
6	-0.0207	11.9 %	0.0707	4.4 %



In the table the values are compared against the original model. The increase in vertical displacement is 10 – 14% and in horizontal 4 – 5%. The resulting sheet displacement at the punching center is found as in Table 13 below:

Table 13. Displacement at punching center (cut outs and no bracing)

$x$ (mm)	$y$ (mm)	$\sqrt{x^2 + y^2}$ (mm)
0.037317	0.005157	0.037672

The result for the total displacement is 5.2% more than in the model without cut outs.

Same cut outs were also tested in the model with diaphragm bracing. There the decline in stiffness was the same order of magnitude as without bracing. Although torsional stiffness is reduced by the cut outs, the model with diaphragm bracing still remains stiffer against torsion compared to the one without bracing. The gap in the horizontal displacement, however, increased from the initial 2% to roughly 7% as Table 14 below shows:

Table 14. Z- and y-displacement with cut outs and diaphragm bracing compared to the original model without cuts out or bracing

Node	$\Delta z$ (mm)	% change	$\Delta y$ (mm)	% change
1	0.0132	-5.0 %	0.0286	6.7 %
2	-0.0117	-6.4 %	0.0286	6.7 %
3	0.0171	-9.0 %	0.0485	7.8 %
4	-0.0145	-11.0 %	0.0485	7.8 %
5	0.0210	-5.8 %	0.0719	6.2 %
6	-0.0172	-7.0 %	0.0719	6.2 %

The resulting sheet displacement at punching center is shown in Table 15 below:

Table 15. Displacement at punching center (with cut outs and diaphragm bracing)

$x$ (mm)	$y$ (mm)	$\sqrt{x^2 + y^2}$ (mm)
0.037666	0.002073	0.037722

Compared to Table 13 (cuts outs and no bracing), diaphragm bracing didn't make any noticeable improvement in the sheet displacement.

#### 4.4.4 Increasing the side wall thickness

Figure 42 shows results with the side wall thickness ( $t_1$ ) increased to from 25 to 30 mm.

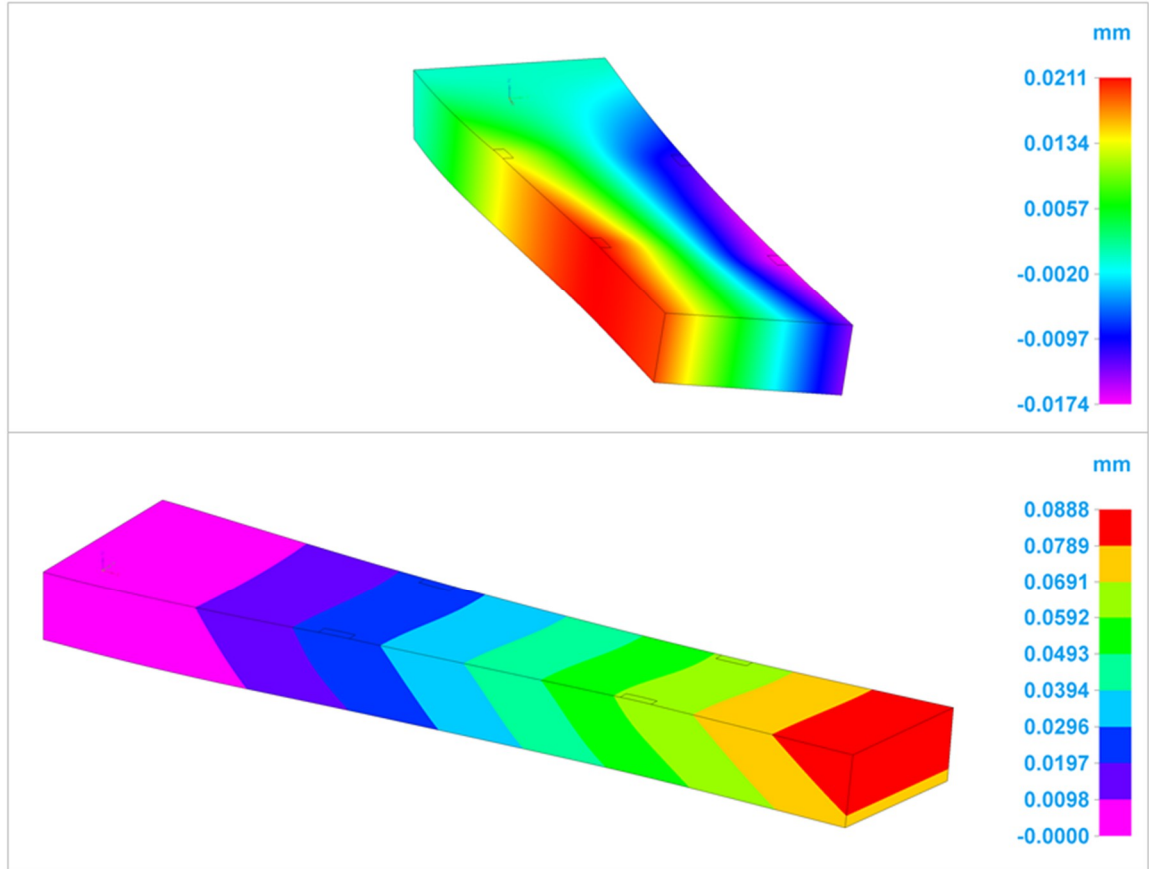


Figure 42. Z- and y-displacement with  $t_1 = 30$  mm (Solid Edge® 2019)

The simulation model is here otherwise identical with the original model but the side wall thickness ( $t_1$ ) has been raised from 25 to 30 mm. Displacement at the nodes is shown in Table 16 below:

Table 16. Z- and y-displacement with  $t_1 = 30$  mm and comparison to the original model

Node	$\Delta z$ (mm)	% change	$\Delta y$ (mm)	% change
1	0.0129	-7.2 %	0.0249	-7.1 %
2	-0.0115	-8.0 %	0.0249	-7.1 %
3	0.0177	-5.9 %	0.0416	-7.6 %
4	-0.0152	-6.7 %	0.0416	-7.6 %
5	0.0210	-5.8 %	0.0622	-8.1 %
6	-0.0174	-5.9 %	0.0622	-8.1 %

Results show that from the tested models, this is the only one with notable improvement in the horizontal displacement. The resulting sheet displacement at the punching center is found as shown in Table 17:

Table 17. Sheet displacement at the punching center (with  $t_1 = 30$  mm)

$x$ (mm)	$y$ (mm)	$\sqrt{x^2 + y^2}$ (mm)
0.032446	0.004721	0.032788

The total displacement is 8.4% less than in the original model (Table 7).

## 5 Analysis of results

In the analytical calculations the results for the transverse displacement are as anticipated: As the width increases, the bending stiffness increases rapidly. When the section width increases from 400 mm to 600 mm, the bending deflection is already reduced by 60%. At the same time the cross-sectional area (and therefore the weight) of the section is increased only 29%. The portion of shear deflection in the total transverse deflection grows by the section width as every increment in width has more powerful impact on bending stiffness compared to shear stiffness. In the 400 mm wide section the portion of shear deflection is 7.5%, whereas in the widest section ( $w = 1000$  mm) the portion of shear is almost 26% of the total transverse deflection.

For torsion deflection both Saint-Venant and warping torsion were used. The maximum difference between the two methods was in the widest section, where warping torsion gave 7.1% smaller result for the angle of twist. The difference can be considered relatively small when taking into account the somewhat extreme dimensional proportions of the frame. The small difference between two methods is a consequence of the use of a closed hollow section, where the warping effect is typically quite mild. In the literature research it was found that the formula for the warping constant for a RHS section isn't often given at all as the warping phenomena is seen so negligible. When comparing the torsion induced movement at the reference height (480 mm from the centroid) to the transverse displacement caused by bending and shear, it was concluded that any increase in width of the section had more significant effect to the flexural stiffness than torsional stiffness as the share of torsion induced transverse displacement grew by each increment in the width of the cross-section.

From the results for the sheet displacement at the punching center can be noted, that the rotation of the cross-section according to the flexure curve compensates for the transverse displacement caused by bending, shear and torsion. In three most narrow frames the rotation actually overshoots the compensation so that the final position of the sheet is on the negative side of the y-axis. From the results can be also concluded that the change in the x-coordinate, which was dominant in the position error, depends not only on the stiffness or length of the frame, but also how the frame centroid is located in reference to the punching center: If its

origin would be located further away from the x-z –plane of the global coordinate system (punching center), the movement in x-direction per angle degree of  $\beta$  would be greater. This would be the case if the specification for the maximum sheet width would change to a next bigger one and the fixed frame location would therefore be shifted further away from the x-y –plane of the punching center. So, in a system with similar masses (= similar deflection) but a wider sheet, the error in x-direction would increase and correspondingly, the compensating movement in y-direction (opposite to the load) caused by the rotation would be slightly less. The described arrangement is illustrated in Figure 43 below:

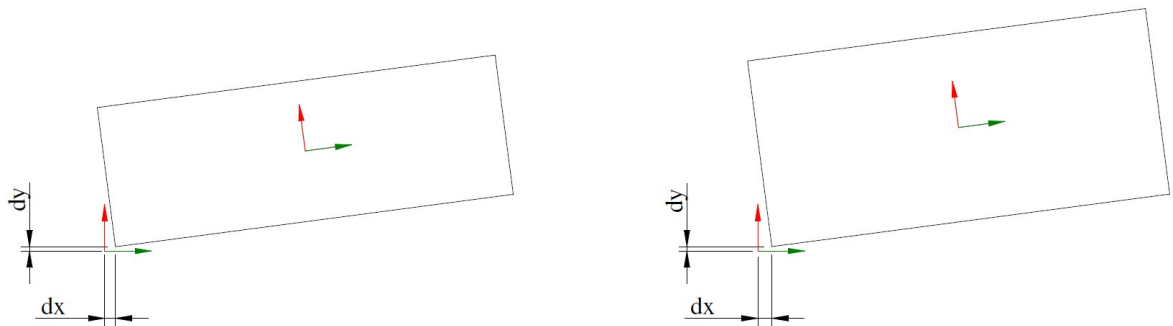


Figure 43. Effect of the reference frame position to the change in x- and y-coordinates during rotation

In the picture is shown two sheets of equal length and equal rotation angle, but the left one being 1.5 meters and the right one 2 meters wide. The centroid of the fixed frame is here positioned according to the sheet size, so the rotation axis is located further away from the punching center x-y –plane, which effects to the ratio of x- and y-displacement per rotation angle.

In the FEM analysis of the simplified model ( $L \sim 2150$  mm) the result for transverse displacement (Figure 30, page 51) was within 3% compared to the analytical result. Although the *slope of the deflection curve* in the analytical calculations and the *nodal rotation* in FEM are different definitions and can't be directly compared to each other, the maximum angle at the sides of the FEM model (Figure 31, page 51) matched almost exactly the slope of the deflection curve. The nodal rotation, however, decreased right after the side plates when moving towards the centroid of the section: This is consistent with Figure 10

(page 20) where the shear stress causes the cross-section to diverge from a perpendicular angle in respect of the deflection curve between the free surfaces.

For the rotation due to torsion (Figure 32, p. 52) the FEM result was closer to Saint-Venant solution than warping torsion, when the angle of twist was calculated based on the vertical displacement at the sides of the section. There the angle of twist was calculated 0.00240 degrees, which is 2% more than Saint-Venant torsion and 8% more than the result from warping torsion. With diagonal bracing (Figure 34, p. 54) the torsion deflection was reduced by 8% in a single diagonal and 15% in a double diagonal bracing. The improvement achieved with double diagonal bracing equals roughly the difference in torsional stiffness between 900 mm and 1000 mm wide sections.

In the model with increased definition (Figure 38, page 59) the use of single diagonal bracing improved torsional rigidity 15 – 23%, when the vertical movement of the selected nodes were compared to the model without bracing. The diaphragm bracing improved similar results by 14 – 18%. When comparing the weight added by the two bracing methods, the diaphragm bracing seems to be more effective in this particular simulation assignment as it raised the weight by approximately 5.3% (for 14 – 18% improvement), whereas single diagonal bracing increased the weight by 14.8% (for 15 – 23% improvement). However, it should be noted that the use of diagonal bracing was pictured in the referenced material (Blodgett 1972, p. 2.10-18) as a part of an open build-up frame *without* top and bottom plates (Figure 18, page 31). There the achieved effect was in a completely different scale and in favour to diagonal bracing. When used in a ladder type frame structure with open top/bottom, the diagonal bracing was reported to provide multiple times greater improvement in torsional rigidity per added weight than diaphragm bracing (Blodgett 1972, p. 2.10-18).

The distortion of the cross-section was assessed by calculating the difference in diagonals taken from nodes 3 and 4 to the opposite corners. When compared to the model with diaphragm bracing there was some S-shape distortion visible in the model without bracing (Figure 40, page 62). The difference in diagonals was there calculated 0.00972 mm. However, when measured with the additional torque load removed, the difference in diagonals was 0.01834 mm, which is almost 2 times more than in the simulation with all the

loads present. The relative order of the diagonal lengths also changed between the simulations. The distortional behaviour of the section is shown in Figure 44:

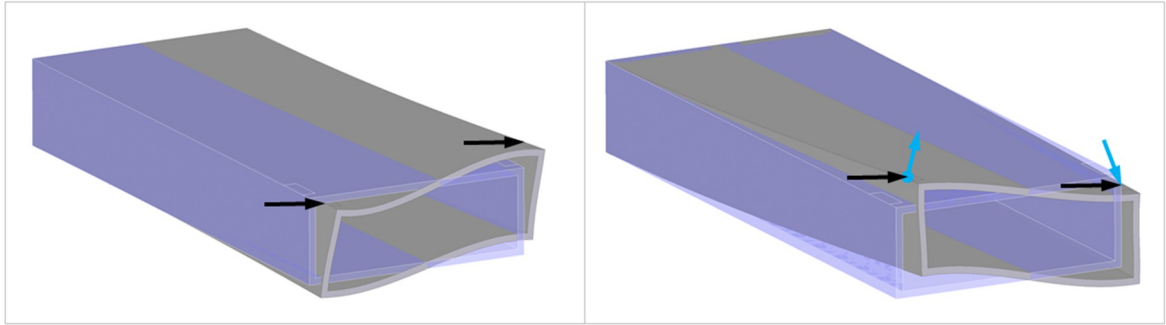


Figure 44. Distortion of a cross-section (Solid Edge® 2019, modified)

On the left is shown the simulation where only the transverse force is applied. The asymmetric force distribution causes bottom plates to deform into S-shape and the section into a parallelogram. On the right is the same model but with the additional torque also applied. The torque acts against the initial distortion so that the final distortion has smaller magnitude and also opposite direction. It should be noted that the loads and boundary condition (cantilever beam) are here applied according to the application, so the picture includes also bending and torsion deformation in addition to distortion.

When cut outs were added to the sides of the frame the vertical displacement at the reference nodes increased 10 – 14% and the horizontal displacement around 4 – 5%. By adding the diaphragm plates, the torsional stiffness could be restored so that results for vertical displacement were still better than in the original model (without cut outs), but the bracing didn't improve the horizontal displacement: It actually grew slightly at the measured nodes. The reason to slight increase in nodal displacement could be related to the distortion of the unbraced section which effects the displacement of these specific nodes, but the issue wasn't investigated more deeply as the difference is yet quite small and didn't recur as such in the total displacement at the end of the frame.

In order to assess the sheet displacement at the punching center according to the results from FEM, and to do it without modelling up the whole sheet positioning system, coordinates measured at specified nodes were used as a basis for the displacement calculations. The rotation around x-axis was defined by the slope of a line placed through nodes 3 – 4 which

were placed midway between the load points. Similarly, the rotation around z-axis was defined by a line through nodes 1 – 5 which represent the positions of linear carriages fixed beneath a sub frame which holds the sheet. The y-coordinate in the vector  $V_L$  was calculated based on the transverse displacement in the nodes 3 – 4: The value in these nodes was selected being a more conservative choice rather than estimating the displacement at the centroid of the cross-section. The results for different models are gathered in Table 18 below:

Table 18. Displacement at punching center

	$x$ (mm)	$y$ (mm)	$\sqrt{x^2 + y^2}$ (mm)
No bracing, no cut outs	0.0356	0.0040	0.0358
Diaphragm bracing	0.0359	0.0013	0.0359
Diagonal bracing	0.0351	0.0003	0.0351
Cut outs, no bracing	0.0373	0.0052	0.0377
Cut outs, diaphragm bracing	0.0377	0.0021	0.0377
No bracing, $t_1=30$ mm, $t_2=25$ mm	0.0324	0.0048	0.0328

From the results can be seen that in all sections the change in x-coordinate determines almost completely the total displacement as the change in y is an order of magnitude smaller. The results also show that either one of the bracing methods (diaphragm or diagonal) didn't have much effect on the displacement at the punching center as they both increase primarily the torsional stiffness, which affects mainly to the y-coordinate. Cut outs in the side plates increased the total displacement by 5%. In the last row is shown the model with increased side wall thickness ( $t_1 = 30$  mm) where the total displacement is 8.4% less compared to the original model. The 5 mm of added material in the side walls increased the total weight of the frame by 4.8%, which makes it the most effective choice in decreasing the sheet displacement at the punching center when compared to the two other bracing methods.



## 6 Conclusions

In the structural analysis of this thesis it was found that with the dimensions used, the bending deformation is the dominant factor in achieving the best accuracy at the punching center. Design against bending deformation calls for the placement of material as far away as possible from the neutral axis. So, if the displacement at the punching center should be further decreased, it could be done either by increasing the width of the cross-section or if not possible, by increasing the wall thickness of the side plates. The shear deformation accounted up to 26% of the total transverse deflection in the widest section, so it was justifiable to include in the calculations. Contrary to bending stress, shear stress induced by a transverse load is carried also by the material at the centroid of a cross-section, where the shear stress actually reaches its peak. Correspondingly, the shear stress in the top and bottom flanges of a section is almost negligible compared to the shear stress in the web plate(s). The transverse displacement at the point of load didn't translate as such at the punching center though: As the frame deflects, the cross-section also rotates according to the deflection curve, which causes the sheet to move in opposite direction to the load at the punching center. This compensates for the transverse displacement caused by bending, shear and torsion, so that the positioning error at the punching center was measured mainly in the longitudinal direction of the frame.

In torsion deflection the maximum difference between Saint-Venant and warping torsion was found 7.1% in the widest section, so the assumption often found in the literature that the warping phenomena in a closed rectangular section is usually negligible seems justifiable as the widest section had already quite extreme proportions ( $L/H \sim 2.2$ ) yet the difference was still well under 10%. In the design against torsion, the most important guideline is to use a closed section whenever possible, which was done also here as the torsional stiffness it provides is in a whole different scale when compared to an open one with similar dimensions.

When comparing the results from FEM and analytical calculations it was found that both gave almost identical values for the transverse deflection. The torsion deflection results from FEM and analytical calculations are a bit more challenging to compare against each other, but when estimating the angle of twist by the vertical moment at the sides of the FEM model,

the result matched almost exactly with Saint-Venant torsion. The positioning error calculated according to FEM was found 24% bigger than the analytical result. The difference can be considered yet admissible, as the results still positions before the next narrower section candidate. The main reason for the bigger result in FEM was the greater rotation angle around the z-axis, which was approximated by calculating the slope of a straight line placed between nodes which represented the linear carriage positions.

The additional bracing methods tested in FEM improved mainly the torsional stiffness, so the reduced transverse displacement at the point of load due to smaller angle of twist had only negligible effect on the sheet displacement at the punching center. From the two bracing methods, the diaphragm bracing was found to be more effective to increase the torsional stiffness in this particular assignment than diagonal bracing. The diaphragm bracing also restricted the distortion of the cross-section, although it wasn't found to be a major issue in the load case as the effect of the transverse load and torsional load partly cancelled each other out. The cut outs tested at the sides of the frame didn't affect the sheet displacement too much, although they caused a local degradation of structural stiffness which could be mainly seen as a greater angle of twist. Examining the effect of these structural modifications are examples of research problems that could be assessed only by FEM.

A cantilever beam was used as a boundary condition in both the FEM and analytical calculations to keep the focus only on the frame itself. Connection at the root plays a crucial role in the structural behavior of the system, so the next step in the design process could be the modelling of the fixing of the frame and examining how it performs under the strain. It would be equally important to investigate the complete force chain from the sheet to the punching center in order to find any possible weak links in the system; a weak connection element along the force chain could dilute the whole system making the rigidity of all other elements more or less redundant. A dynamic analysis could also come into question at some point. A time response analysis of the complete system would probably turn out to be quite challenging to perform, but examining even the natural frequencies and mode shapes of some individual parts or subassemblies could give some perception of the mass – stiffness ratio of the construction.

## References

- Bauchau, O.A. & Craig, J.I. 2009. *Structural Analysis: With Applications to Aerospace Structures*. New York, USA: Springer. 943 p.
- Björk, T., Ahola, A. & Skriko, T. 2020. On the distortion and warping of cantilever beams with hollow section. *Weld World* 64, p. 1269 – 1278.
- Blodgett, O. 1972. *Design of Welded Structures*. Cleveland, USA: The James F. Lincoln Arc Welding Foundation. 834 p.
- Da Silva, V. 2006. *Mechanics and Strength of Materials*. Berlin, Germany: Springer. 529 p.
- Gere, J. M. & Goodno, B. J. *Mechanics of Materials*. 2012. Brief edition. USA: Cengage Learning. 620 p.
- Gross, D., Hauger, W., Schröder, J., Wall, W. & Bonet, J. 2011. *Engineering Mechanics 2: Mechanics of Materials*. Berlin, Germany: Springer. 308 p.
- Karhunen, J., Lassila, V., Pyy, S., Ranta, A., Räsänen, S., Saikkonen, M. & Suosara E. 2012. *Lujuusoppi*. Helsinki: Otatieto. 571 p.
- Kermani, B. & Waldron, P. 1993. Analysis of continuous box girder bridges including the effects of distortion. *Computers & Structures*, 47(3), p. 427 – 440. Great Britain: Pergamon Press Ltd.
- Hughes, A., Iles, D. & Malik, A. 2011. *Design of Steel Beams in Torsion*. UK: Steel Construction Institute. 136 p.
- Outinen, H. & Salmi, T. 2004. *Lujuusopin perusteet*. Tampere: Pressus Oy. 464 p.

Parnes, R. 2001. Solid Mechanics in Engineering. Chichester, England: John Wiley & Sons Ltd. 748 p.

Pennala, E. 2002. Lujuusopin perusteet. 11<sup>th</sup> edition. Helsinki: Otatieta. 400 p.

Rubin, H. 2005. Wölbkrafttorsion von Durchlaufträgern mit konstantem Querschnitt unter Berücksichtigung sekundärer Schubverformungen. Stahlbau, 74: p. 826-842. Berlin: Ernst & Sohn Verlag für Architektur und technische Wissenschaften GmbH & Co.

Salmi, T. & Pajunen, S. 2010. Lujuusoppi. Tampere: Pressus Oy. 462 p.

Singh, D. K. 2021. Strength of Materials. 4<sup>th</sup> edition. Switzerland: Springer Nature Switzerland AG. 905 p.

Siciliano, B., Sciavicco, L., Villani, L. & Oriolo G. 2009. Robotics: Modelling, Planning and Control. London, UK: Springer-Verlag. 644 p.

Timoshenko, S. 1940. Strength of Materials, Part II: Advanced Theory and Problems. 2<sup>nd</sup> edition. New York, USA: Van Nostrand Company. 510 p.

Timoshenko, S. & Gere, J. 1963. Theory of Elastic Stability. 2<sup>nd</sup> edition. New York, USA: McGraw-Hill. 541 p.

Valtanen, E. 2019. Tekniikan taulukkokirja. 22<sup>nd</sup> edition. Jyväskylä: Genesis-Kirjat Oy. 1320 p.

Zhu, Y., Nie, X., Wang, J., Tao, M. & Fan, J. 2020. Multi-index distortion control of steel-concrete tub girders considering interior cross-frame deformation. Engineering Structures, volume 210. 17 p.